

## Supporting Information

### **Observation of polar order and thermochromic behaviour in a chiral bent-core system exhibiting exotic mesophases due to superstructural frustration**

Vidhika Punjani,<sup>a‡</sup> Golam Mohiuddin,<sup>a‡</sup> Supreet Kaur,<sup>a</sup> Raj Kumar Khan,<sup>b</sup> Sharmistha Ghosh,<sup>b</sup> and Santanu Kumar Pal<sup>\*a</sup>

<sup>a</sup>Department of Chemical Sciences, Indian Institute of Science Education and Research (IISER) Mohali, Sector-81, Knowledge City, Manauli 140306 (India)  
E-mail: [skpal@iisermohali.ac.in](mailto:skpal@iisermohali.ac.in); [santanupal.20@gmail.com](mailto:santanupal.20@gmail.com)

<sup>b</sup>Department of Physics, University of Calcutta, 92 Acharyya Prafulla Chandra Road, Kolkata-700009

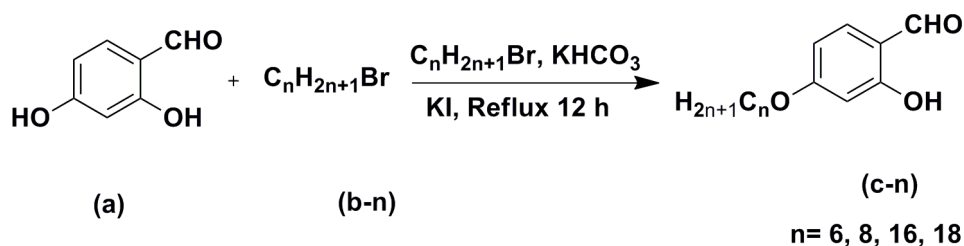
Table of contents:

1. Synthesis
2. Chemical characterization
3. UV-visible studies
4. IR studies
5. Polarizing optical microscopy
6. Differential scanning calorimetry
7. Temperature dependent X-ray diffraction studies
8. Thermochromism
9. Details of DFT calculations
10. Dielectric Investigations
11. Instrumental
12. References

#### **1. Synthesis:**

##### Step 1.

The synthesis of 4-n-alkoxy-2-hydroxybenzaldehyde was performed by using a modification of the literature procedure to improve the product and yield.

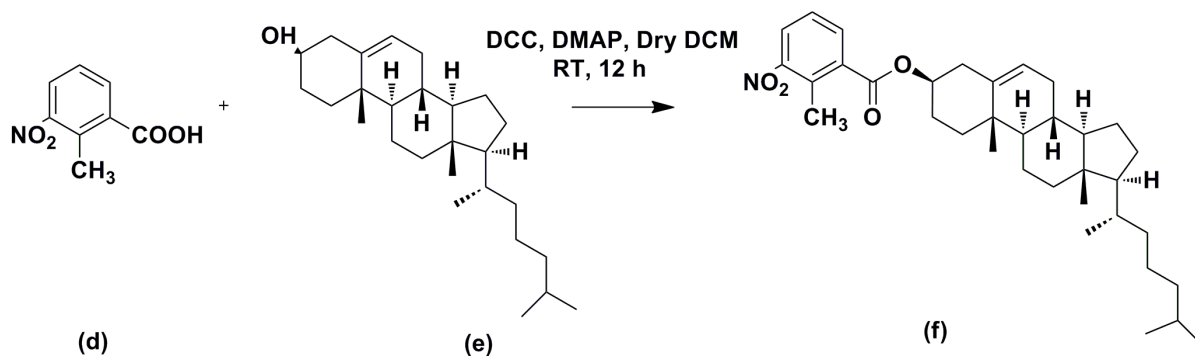


2, 4-dihydroxybenzaldehyde (1 equivalent), 1-bromoalkane (1 equivalent),  $\text{KHCO}_3$  (1 equivalent) and catalytic amount of KI were mixed in dry acetone (250 mL) and the mixture was refluxed for 12 h. It was then filtered hot to remove the insoluble solid. The warm solution was neutralized by adding dilute HCl and extracted twice with  $\text{CHCl}_3$  (100 mL). The combined extract was concentrated to give a purple liquid. The product was further purified by column chromatography using silica gel (60-120 mesh) eluting with a mixture of hexane and chloroform (v/v 1:1) followed by evaporation of the solvent. The product was obtained as a pale yellow liquid. Yield = 60%.

The other homologues with varying the number of carbon atoms (n) in the alkoxy chain (n = 8, 16, 18) were synthesized following the above procedure with appropriate amount of alkyl bromides.

### Step 2.

This step involves the formation of an ester bond between 2-methyl-3-nitrobenzoic acid and cholesterol by DCC/DMAP coupling reaction. Appropriate quantity of methyl substituted nitro benzoic acid (1 equivalent) and cholesterol (1.1 equivalent) were dissolved in dry dichloromethane (DCM) (50 mL) under nitrogen atmosphere and catalytic amount of 4-dimethylaminopyridine (DMAP) was added to the solution. A solution of N,N'-Dicyclohexylcarbodiimide (DCC) (1.25 equivalent) was added to the reaction mixture and the mixture was stirred for 12 h under inert atmosphere at room temperature. The precipitate of Dicyclohexylurea was removed by filtration and the solvent DCM was evaporated to get the crude product. The reaction mixture was separated by column chromatography using silica gel of 60-120 mesh by eluting it with a mixture of hexane and ethyl acetate (v/v 100:1) followed by evaporation of the solvent. The product was obtained as a white solid. Yield = 80%.

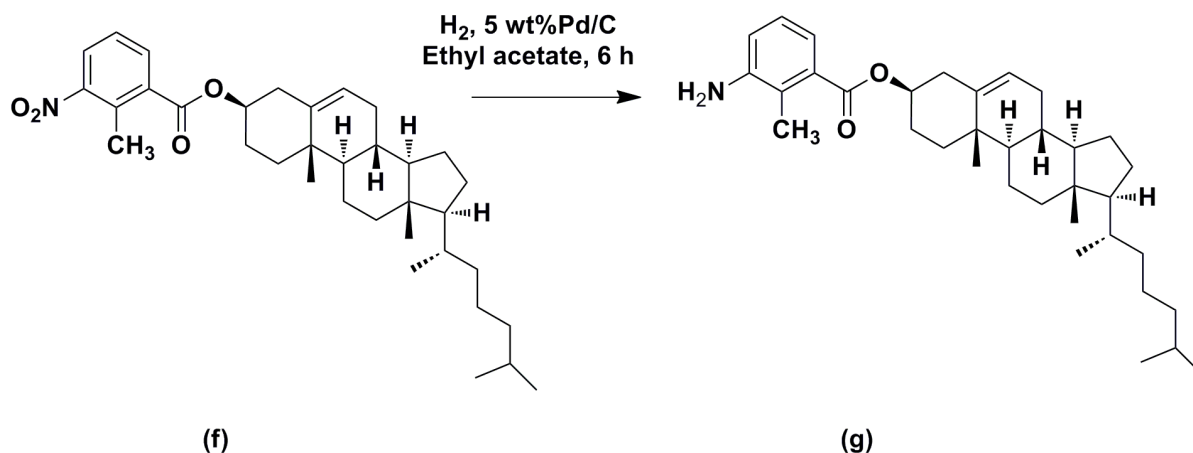


### Step 3.

This step involves the reduction of the nitro compound 'f' from Step 2. Appropriate quantity of nitro compound 'f' was weighed and dissolved in minimum quantity of ethyl acetate. 5wt% of Pd/C was added to the nitro product and the reaction was stirred for 6 h under H<sub>2</sub> atmosphere. The reaction was continuously monitored via TLC and the end point of the reaction also confirmed by TLC. After completion of the reaction, the mixture was then filtered off to remove the black Pd/C and the product was collected by evaporating the solvent *via* rotary evaporator. The product was dried under vacuum. Here it is noteworthy to mention that the -CH=C of cholesterol did not get reduced which has been proved by <sup>1</sup>H-NMR spectrum of compound 'g' by observing a doublet of doublet peak at 5.45-5.46 ppm, a characteristic peak of H atom in -CH=C- bond. The important points to be noted during the reactions are

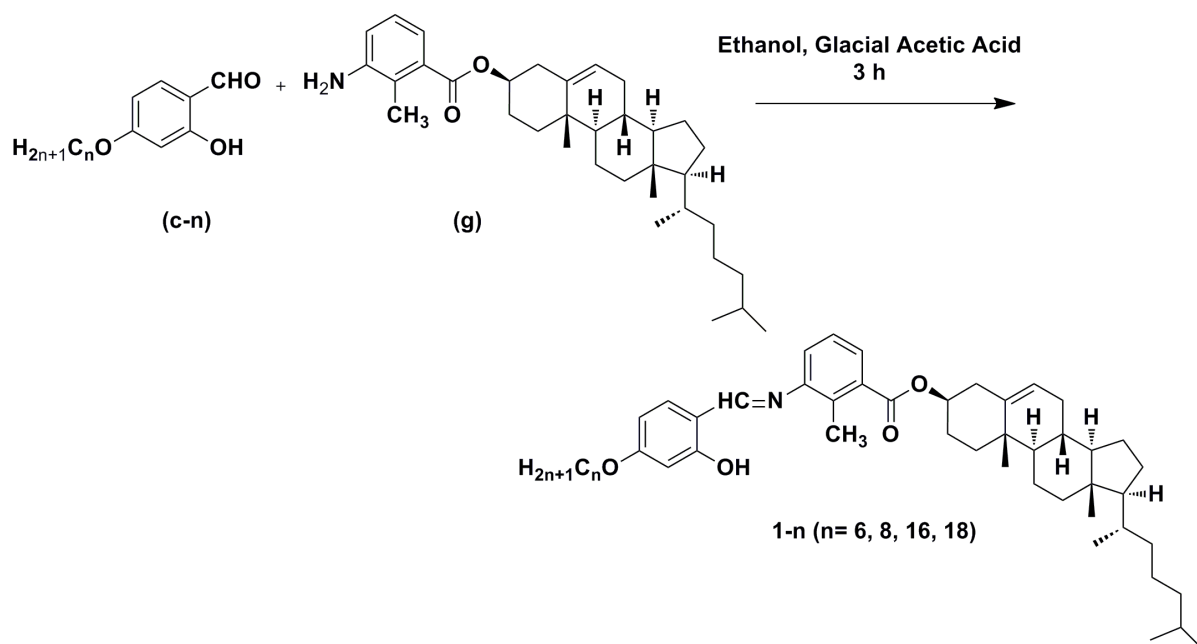
(i) Room temperature (ii) 5 wt% of Pd/C (iii) continuous monitoring *via* TLC and (iv) reaction time 6 hrs.

Yield = 85%.



### Step 4.

The final Schiff base compounds were synthesized following the standard procedure reported earlier by refluxing a mixture of ethanolic solution of 1 equivalent of the 4-n-alkyloxy-2-hydroxybenzaldehyde with 1 equivalent of compound 'g' and few drops of glacial acetic acid as catalyst for 3 h. The precipitated product was purified by repeated recrystallization from absolute ethanol. The final product was obtained as a light yellow solid. Yield = 85%.



## 2. Chemical Characterisation:

**Compound c-6:** Yield = 60 %

**FT-IR:** Intramolecular H-bonding of O-H...N at  $3449\text{ cm}^{-1}$ , C=O stretching band of aldehyde at  $1666\text{ cm}^{-1}$

**$^1\text{H NMR}$  (400 MHz,  $\text{CDCl}_3$ ,  $\delta$  in ppm):**  $\delta = 11.49$  (s, 1H, -OH),  $9.70$  (s, 1H, -CHO),  $7.41$  (d, 1H,  $J = 8.0$  Hz, Ar-H),  $6.53$  (1H, Ar-H),  $6.41$  (d, 1H,  $J = 2.2$  Hz, Ar-H),  $4.00$  (t, 2H,  $J = 8.0$  Hz, -OCH<sub>2</sub>-),  $1.83$ - $1.76$  (m, 2H, -CH<sub>2</sub>-),  $1.49$ - $1.42$  (m, 2H, -CH<sub>2</sub>-),  $1.37$ - $1.32$  (m, 4H, -(CH<sub>2</sub>)<sub>2</sub>),  $0.91$  (t, 3H,  $J = 4.0$  Hz, -CH<sub>3</sub>).

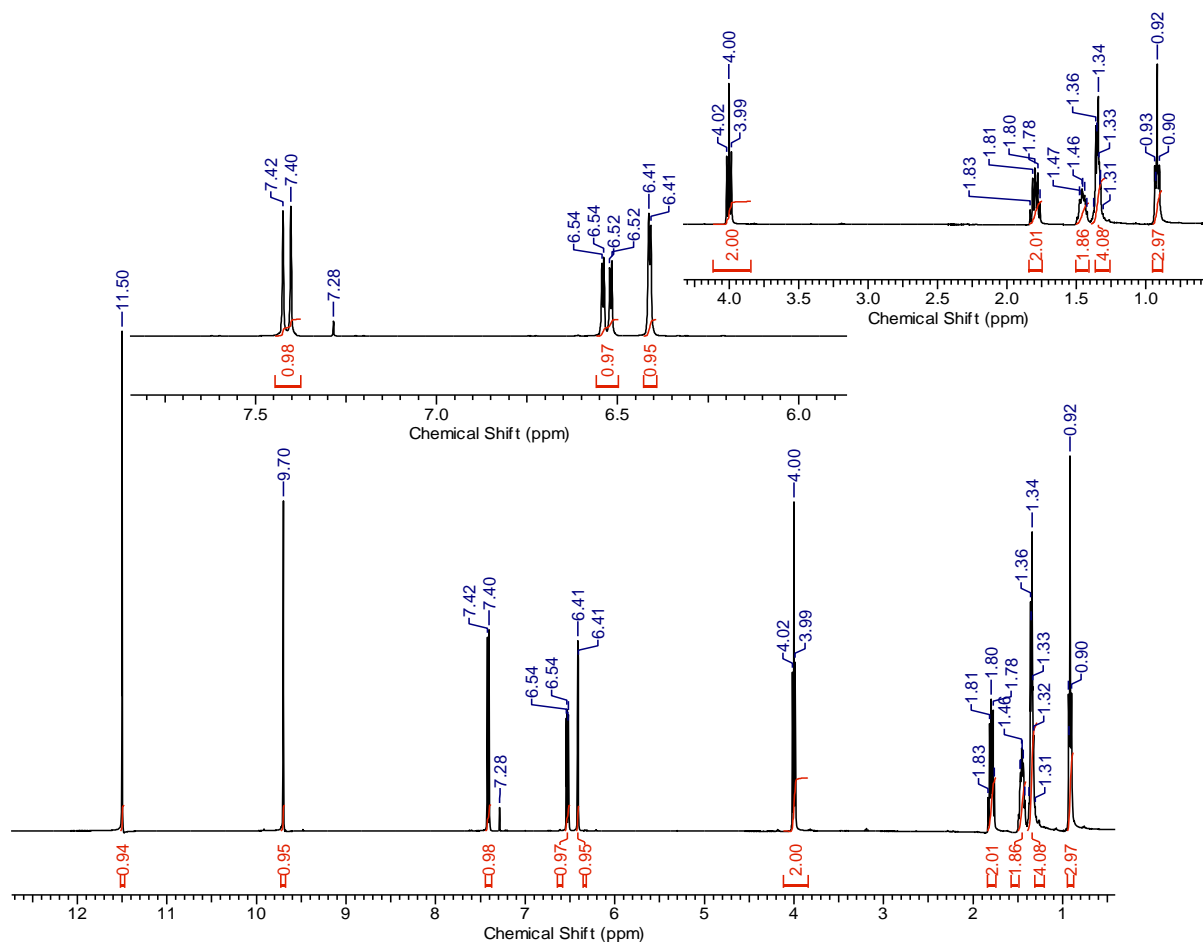


**Figure S1(a):**  $^1\text{H}$  NMR spectrum of compound **c-6**

**Compound c-8:**

**$^1\text{H}$  NMR (400 MHz,  $\text{CDCl}_3$ ,  $\delta$  in ppm):**  $\delta$  = 11.51 (s, 1H, -OH), 9.72 (s, 1H, -CHO), 7.43 (d, 1H,  $J$  = 8.0 Hz, Ar-H), 6.55 (1H,  $J^1$  = 2.2,  $J^2$  = 8.7, Ar-H), 6.43 (d, 1H,  $J$  = 2.1 Hz, Ar-H), 4.01 (t, 2H,  $J$  = 8.0 Hz,  $-\text{OCH}_2-$ ), 1.85-1.78 (m, 2H,  $-\text{CH}_2-$ ), 1.50-1.43 (m, 2H,  $-\text{CH}_2$ ), 1.38-1.30 (m, 8H,  $-(\text{CH}_2)_4$ ), 0.90 (t, 3H,  $J$  = 4.0, 8.0 Hz,  $-\text{CH}_3$ ).

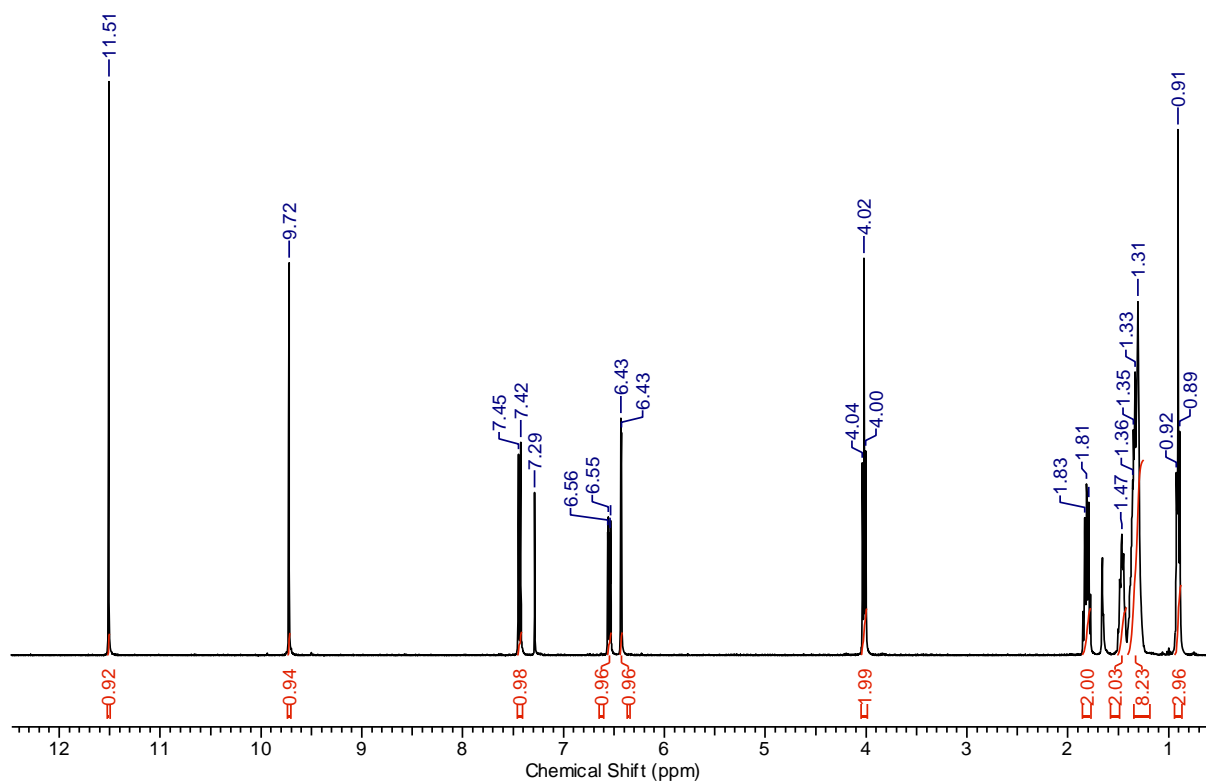


**Figure S1(b):**  $^1\text{H}$  NMR spectrum of compound **c-8**

**Compound c-16:**

**$^1\text{H}$  NMR (400 MHz,  $\text{CDCl}_3$ ,  $\delta$  in ppm):**  $\delta = 11.51$  (s, 1H, -OH), 9.73 (s, 1H, -CHO), 7.44 (d, 1H,  $J = 8.0$  Hz, Ar-H), 6.55 (dd, 1H,  $J^1 = 2.2$ ,  $J^2 = 8.8$ , Ar-H), 6.43 (d, 1H,  $J = 2.1$  Hz, Ar-H), 4.02 (t, 2H,  $J = 8.0, 4.0$  Hz,  $-\text{OCH}_2-$ ), 1.85-1.77 (m, 2H,  $-\text{CH}_2-$ ), 1.50-1.43 (m, 2H,  $-\text{CH}_2$ ), 1.38-1.28 (m, 24H,  $-(\text{CH}_2)_{12}$ ), 0.90 (t, 3H,  $J = 8.0$  Hz,  $-\text{CH}_3$ ).

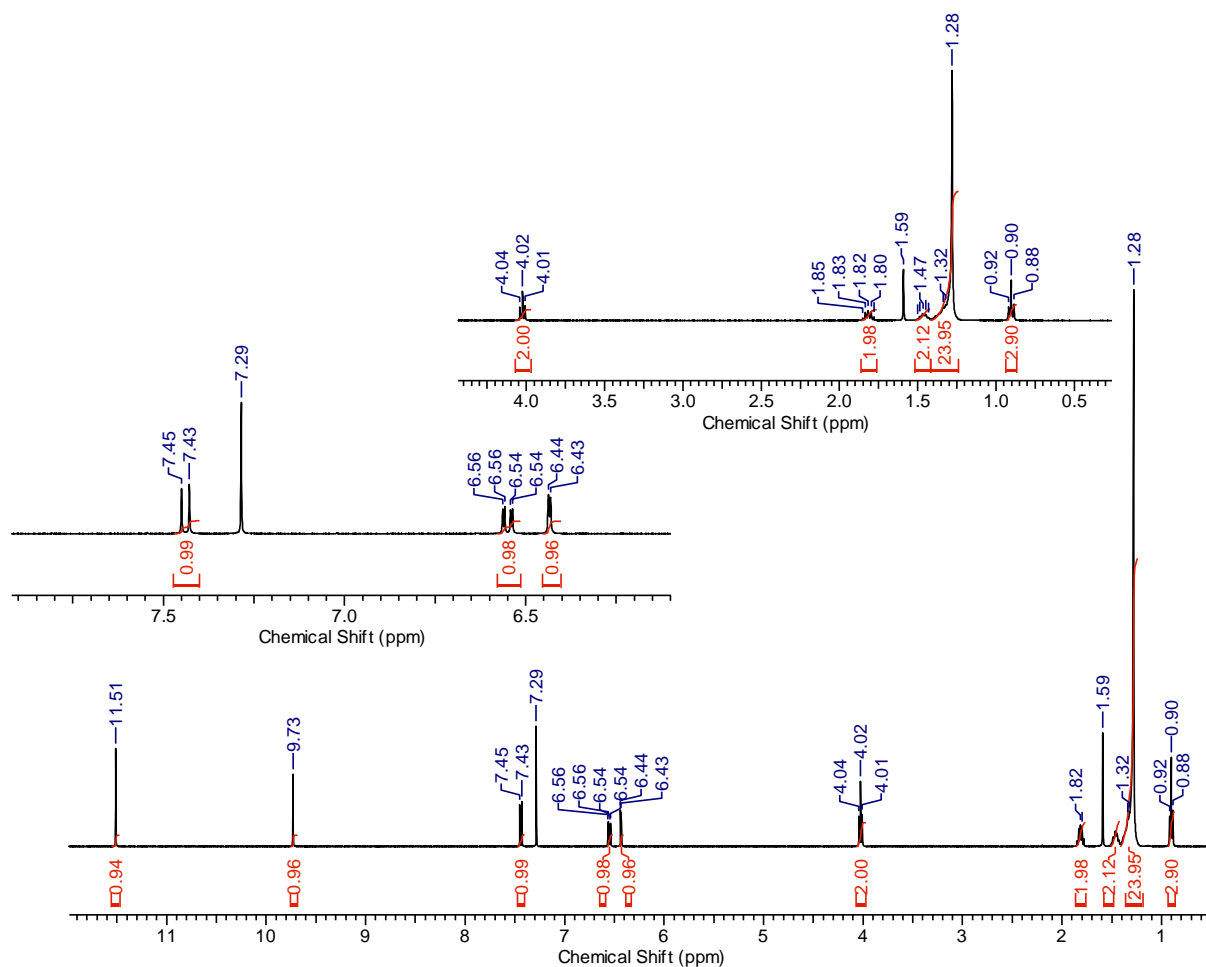


**Figure S1(c):** <sup>1</sup>H NMR spectrum of compound c-16

**Compound c-18:**

**<sup>1</sup>H NMR (400 MHz, CDCl<sub>3</sub>, δ in ppm):** δ = 11.51 (s, 1H, -OH), 9.73 (s, 1H, -CHO), 7.44 (d, 1H, *J* = 8.0 Hz, Ar-H), 6.55 (dd, 1H, *J*<sup>1</sup> = 2.2, *J*<sup>2</sup> = 8.4, Ar-H), 6.43 (d, 1H, *J* = 2.2 Hz, Ar-H), 4.02 (t, 2H, *J* = 8.0 Hz, -OCH<sub>2</sub>-), 1.85-1.78 (m, 2H, -CH<sub>2</sub>-), 1.48-1.43 (m, 2H, -CH<sub>2</sub>-), 1.38-1.28 (m, 28H, -(CH<sub>2</sub>)<sub>14</sub>), 0.90 (t, 3H, *J* = 8.0 Hz, -CH<sub>3</sub>).

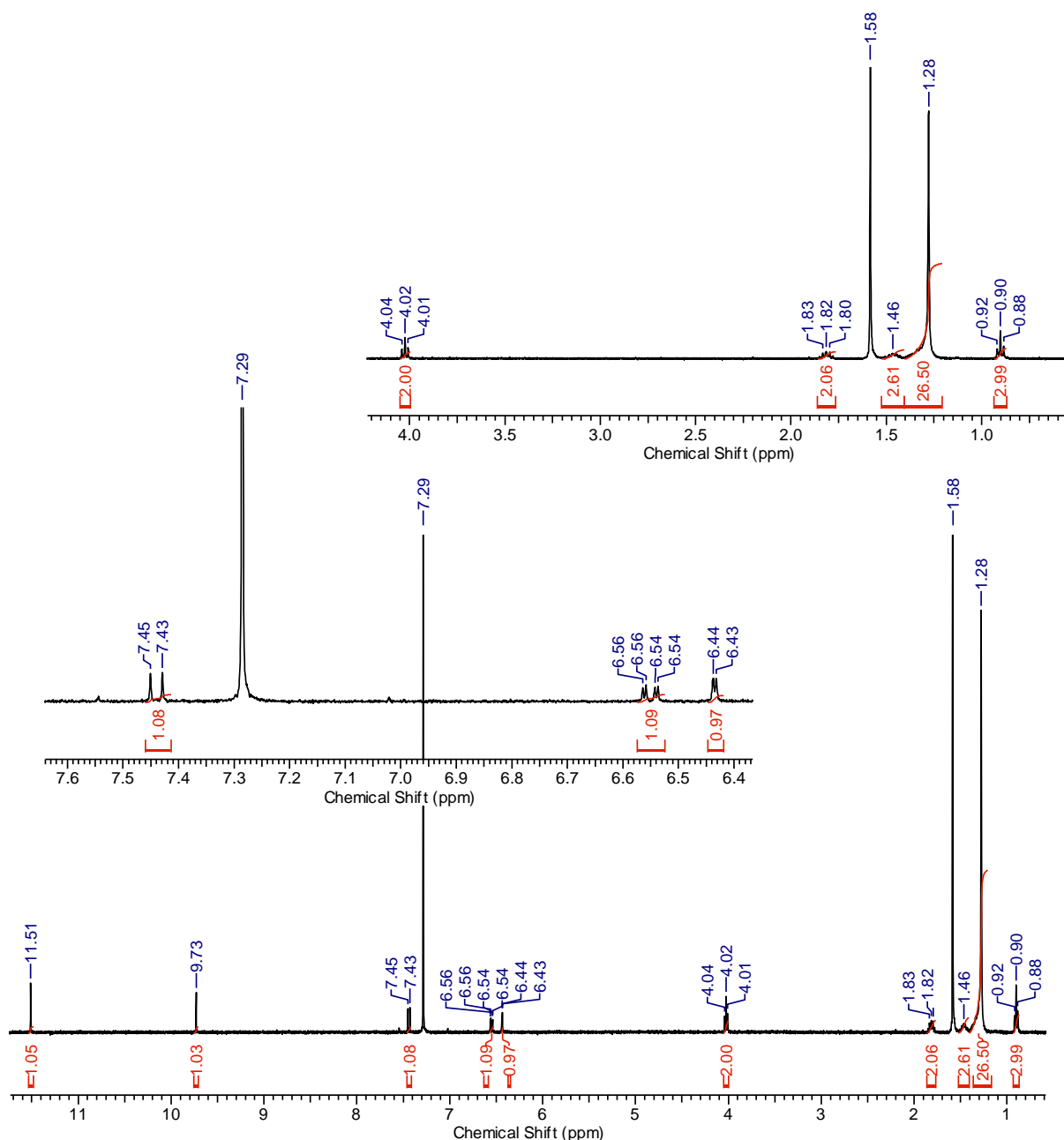
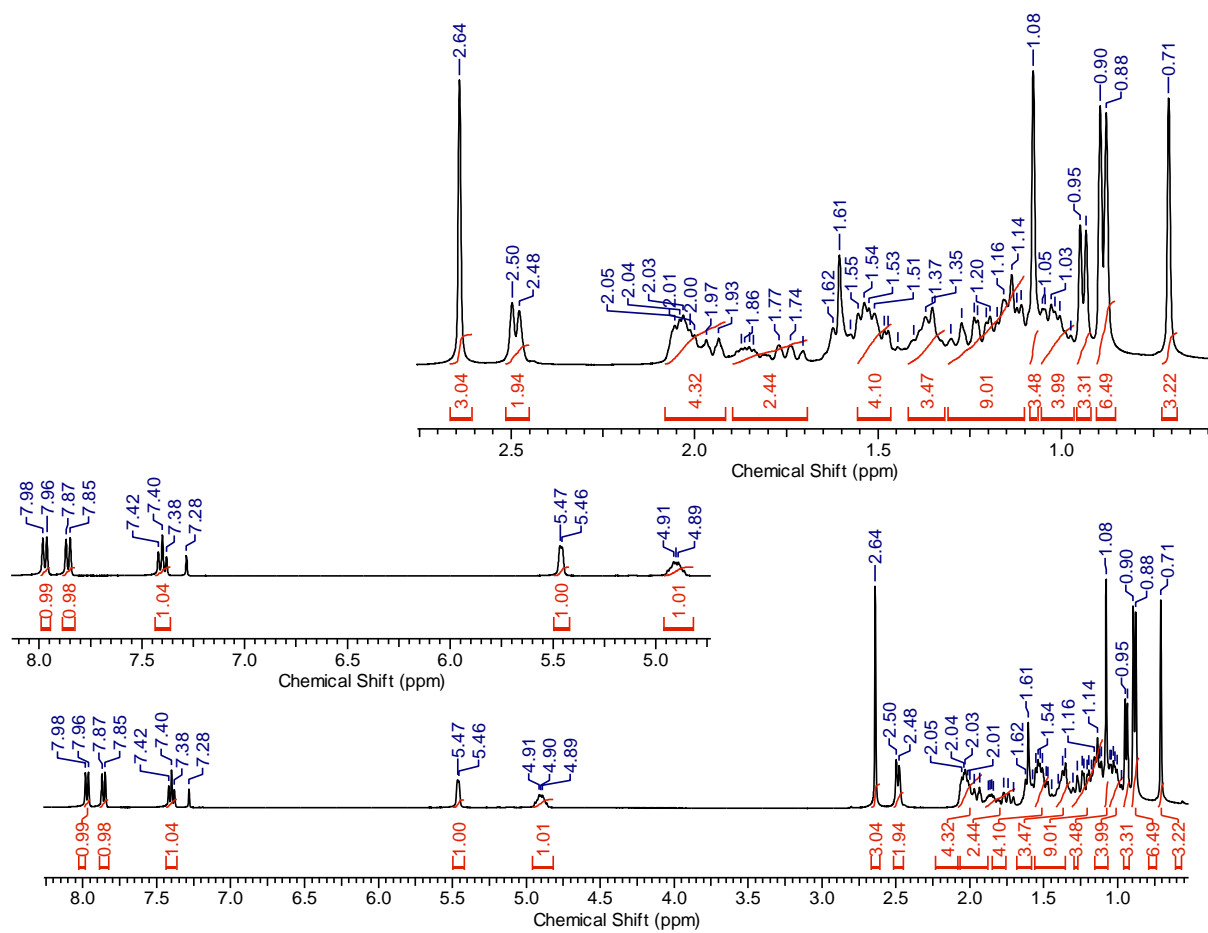


Figure S1(d):  $^1\text{H}$  NMR spectrum of compound **c-18**

**Compound f:**

**$^1\text{H}$  NMR (400 MHz,  $\text{CDCl}_3$ ,  $\delta$  in ppm):**  $\delta = 7.98\text{-}7.96$  (d, 1H,  $J = 8.0$  Hz, Ar-H),  $7.87\text{-}7.85$  (d, 1H,  $J = 8.0$  Hz, Ar-H),  $7.42\text{-}7.38$  (t, 1H,  $J = 8.0$  Hz, Ar-H),  $5.46\text{-}5.45$  (d, 1H,  $-\text{CH}=\text{C}$  in cholesteryl),  $4.94\text{-}4.84$  (1H, m,  $-\text{CH}-\text{O}-$  in cholesteryl),  $2.49\text{-}2.45$  (2H, m,  $-\text{CH}_2$  in cholesteryl),  $2.64$  (s, 3H, Ar- $\text{CH}_3$ ),  $1.07$  (s, 3H,  $-\text{CH}_3$  in cholesteryl),  $0.71$  (s, 3H,  $-\text{CH}_3$  in cholesteryl),  $2.06\text{-}0.71$  (41H, extensive coupling).

**$^{13}\text{C}$  NMR (100 MHz,  $\text{CDCl}_3$ ,  $\delta$  in ppm):**  $\delta = 11.88, 16.28, 18.73, 19.36, 21.06, 22.59, 22.85, 23.85, 24.31, 27.84, 28.04, 28.25, 31.86, 31.93, 35.82, 36.19, 36.64, 36.99, 38.12, 39.53, 39.72, 42.33, 50.02, 56.14, 56.68, 75.69, 123.20, 126.37, 126.44, 132.67, 133.38, 134.34, 139.24, 151.84, 166.03$ .



**Figure S2:** <sup>1</sup>H-NMR spectrum of compound **f**

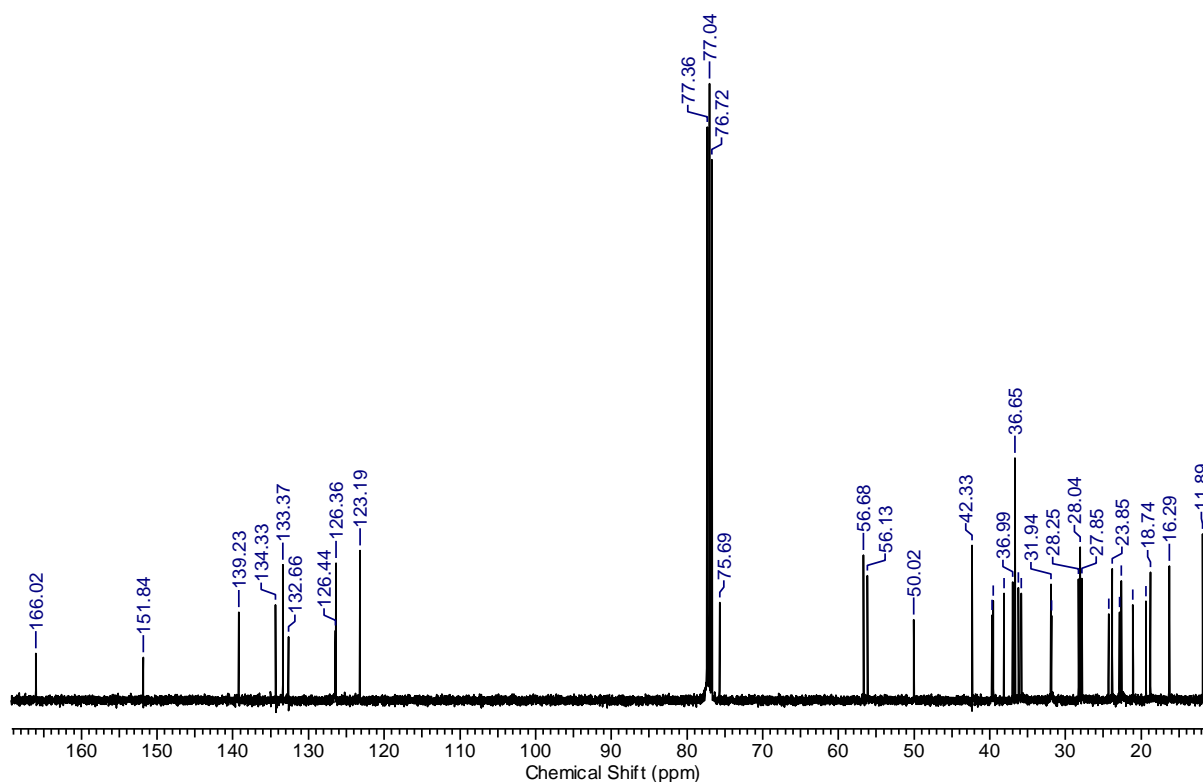


**Figure S3:**  $^{13}\text{C}$  NMR spectrum of compound **f**

**Compound g:**

**$^1\text{H}$  NMR (400 MHz,  $\text{CDCl}_3$ ,  $\delta$  in ppm):**  $\delta$  = 7.22-7.19 (1H,  $J$  = 4.0 Hz, Ar-H), 7.07 (t, 1H,  $J$  = 8.0 Hz, Ar-H), 6.83-6.81 (d, 1H,  $J$  = 8.0 Hz, Ar-H), 5.45-5.44 (d, 1H,  $-\text{CH}=\text{C}$  in cholesteryl), 4.90-4.82 (m, 1H,  $-\text{CH}-\text{O}-$  in cholesteryl), 3.88 (2H,  $-\text{NH}_2$  in cholesteryl), 2.49-2.47 (2H, m,  $-\text{CH}_2$  in cholesteryl), 2.35 (s, 3H, Ar- $\text{CH}_3$ ), 1.07 (s, 3H,  $-\text{CH}_3$  in cholesteryl), 0.71 (s, 3H,  $-\text{CH}_3$  in cholesteryl), 2.05-0.70 (41H, extensive coupling).

**$^{13}\text{C}$  NMR (100 MHz,  $\text{CDCl}_3$ ,  $\delta$  in ppm):**  $\delta$  = 11.88, 13.90, 18.74, 19.39, 21.06, 22.59, 22.86, 23.85, 24.31, 27.89, 28.04, 28.27, 31.88, 31.95, 35.83, 36.20, 36.67, 37.08, 38.21, 39.53, 39.75, 42.33, 50.04, 56.14, 56.70, 74.54, 117.93, 120.15, 122.53, 122.76, 126.09, 132.51, 139.70, 145.40, 168.25.

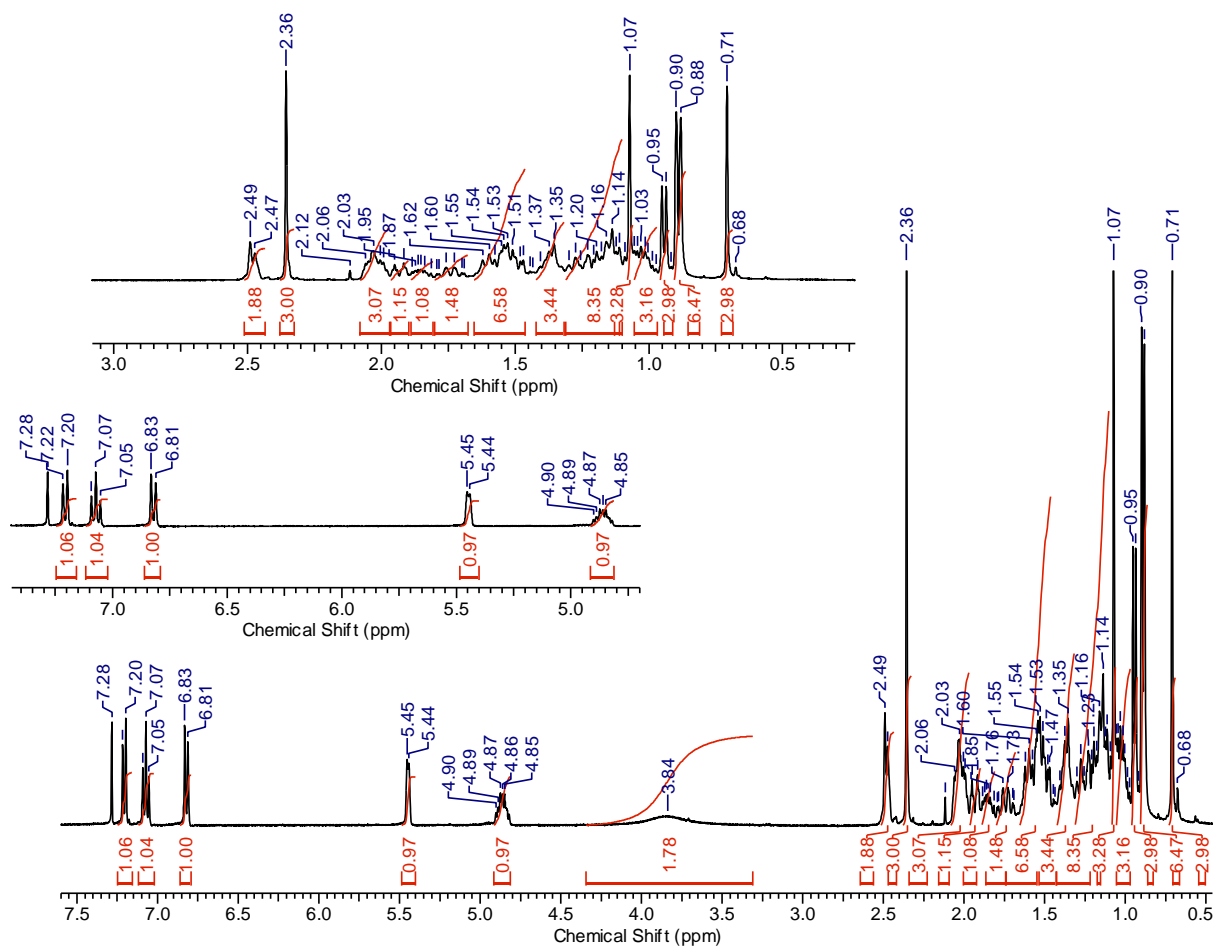
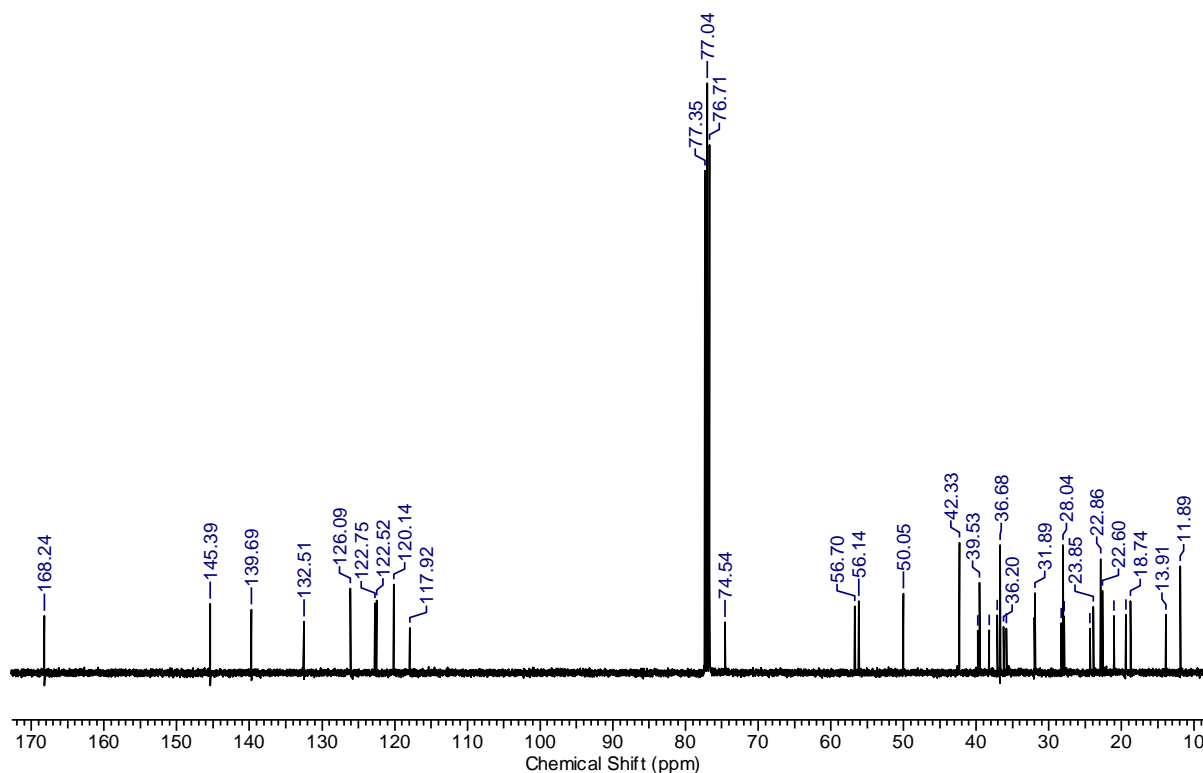


Figure S4:  $^1\text{H}$  NMR spectrum of compound **g**



**Figure S5:**  $^{13}\text{C}$  NMR spectrum of compound **g**

**Compound 1-6:** Yield = 85%

**FT-IR:** Intramolecular H-bonding of O-H...N at  $3170\text{--}3400\text{ cm}^{-1}$ , C=O stretching band of ester at  $1721\text{ cm}^{-1}$ , HC=N stretching of imine at  $1615\text{ cm}^{-1}$

**UV-vis:** 285.78 nm, 337.52 nm

**$^1\text{H}$  NMR (400 MHz,  $\text{CDCl}_3$ ,  $\delta$  in ppm):**  $\delta$  = 13.63 (s, 1H, -OH), 8.43 (s, 1H, -CH=N), 7.68 (d, 1H,  $J$  = 8.0 Hz, Ar-H), 7.32-7.30 (2H, Ar-H), 7.19-7.17 (d, 1H, Ar-H), 6.54-6.51 (m, 2H, Ar-H), 5.46-5.45 (d, 1H, -CH=C in cholesteryl), 4.94-4.84 (1H, m, CH-O- in cholesteryl), 4.03 (t, 2H,  $J$  = 8.0, 4.0 Hz, -OCH<sub>2</sub>-), 2.51-2.44 (2H, m, -CH<sub>2</sub> in cholesteryl), 2.58 (s, 3H, Ar-CH<sub>3</sub>), 1.08 (s, 3H, -CH<sub>3</sub> in cholesteryl), 0.71 (s, 3H, -CH<sub>3</sub> in cholesteryl), 2.5-0.71 (m, 52H, extensive coupling).

**$^{13}\text{C}$  NMR (100 MHz,  $\text{CDCl}_3$ ,  $\delta$  in ppm):**  $\delta$  = 11.89, 14.07, 15.35, 18.74, 19.40, 21.07, 22.59, 22.62, 22.86, 23.85, 24.32, 25.68, 27.91, 28.04, 28.27, 29.04, 31.57, 31.88, 31.95, 35.83, 36.20, 36.68, 37.07, 38.22, 39.53, 39.74, 42.34, 50.05, 56.14, 56.71, 68.31, 74.88, 101.52, 107.69, 113.00, 121.38, 122.89, 126.41, 127.54, 132.56, 132.72, 133.58, 139.59, 149.16, 162.35, 163.72, 163.78, 167.58.

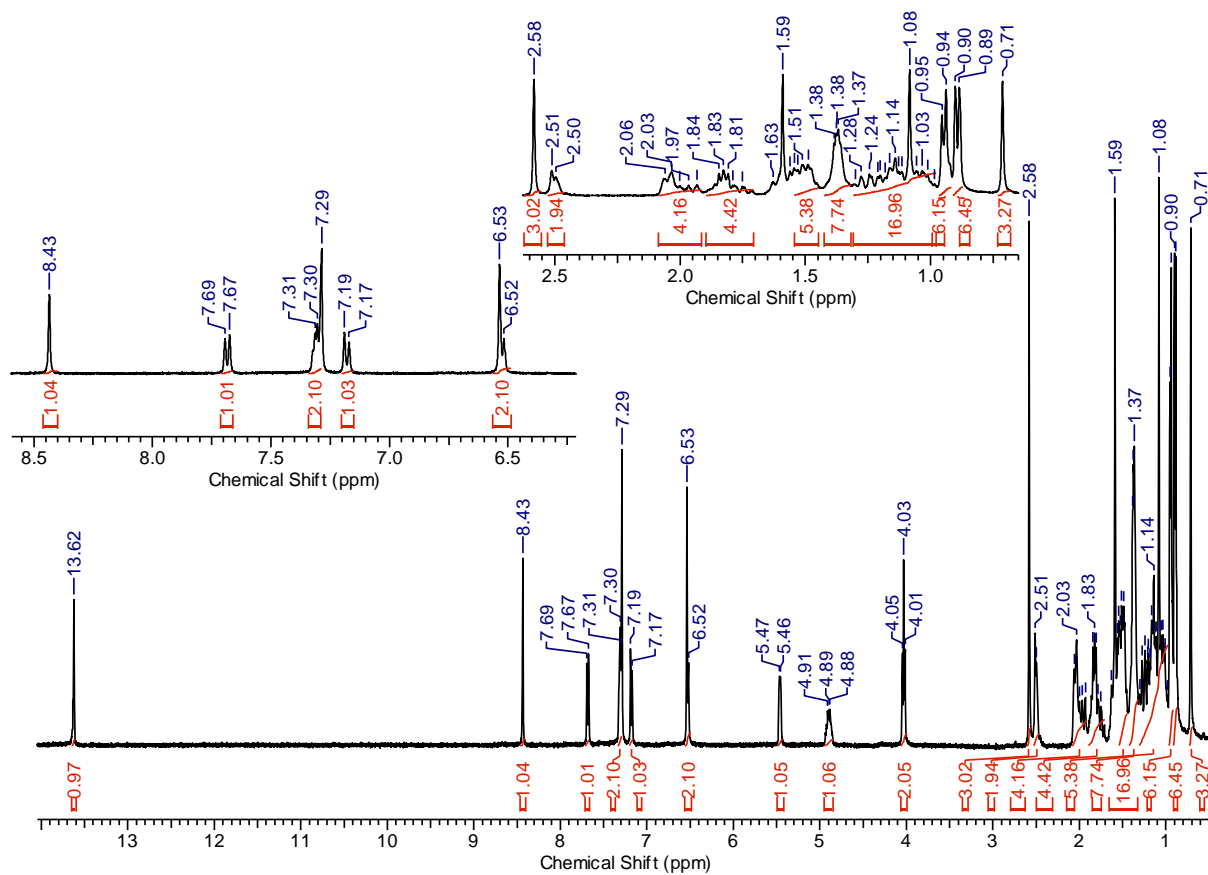


Figure S6:  $^1\text{H}$  NMR spectrum of compound 1-6

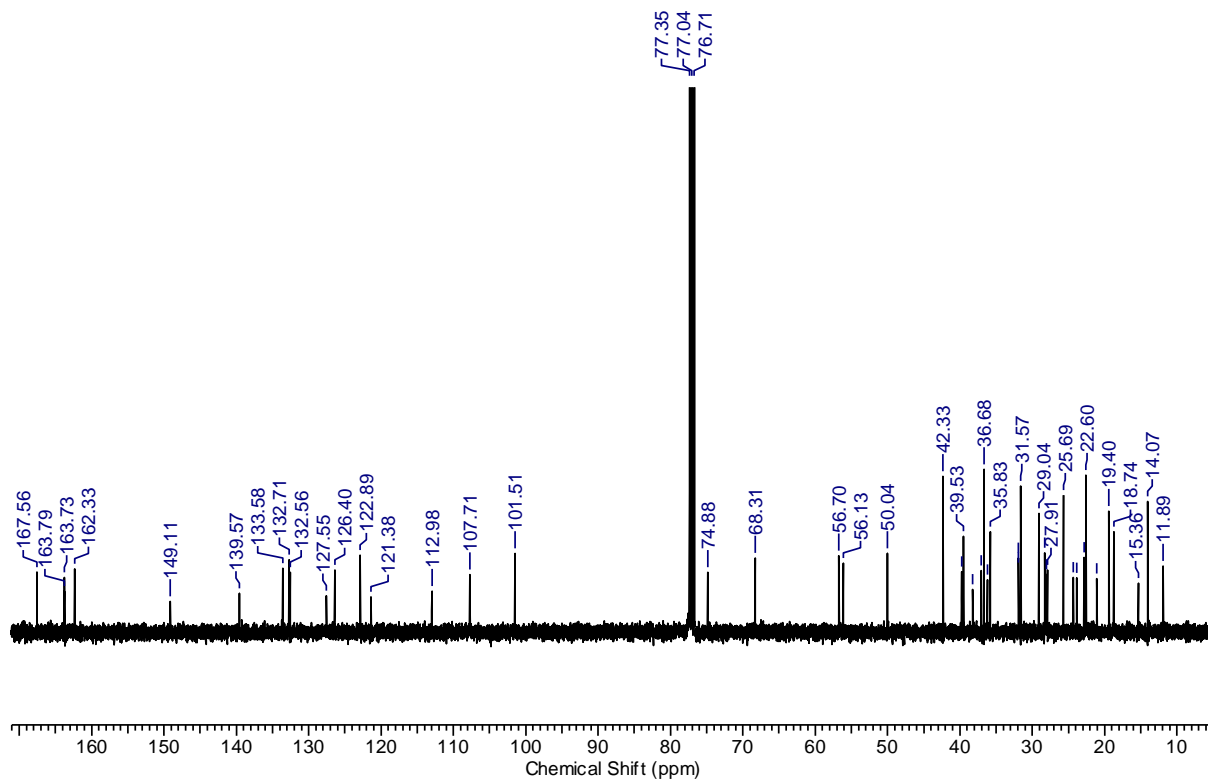


Figure S7:  $^{13}\text{C}$  NMR spectrum of compound 1-6

**Compound 1-8:** Yield = 82%

**FT-IR:** Intramolecular H-bonding of O-H...N at 3170–3400  $\text{cm}^{-1}$ , C=O stretching band of ester at 1721  $\text{cm}^{-1}$ , HC=N stretching of imine at 1615  $\text{cm}^{-1}$

**UV-vis:** 284.97 nm, 338.44 nm

**$^1\text{H}$  NMR (400 MHz,  $\text{CDCl}_3$ ,  $\delta$  in ppm):**  $\delta$  = 13.62 (s, 1H, -OH), 8.43 (s, 1H, -CH=N), 7.68 (d, 1H,  $J$  = 8.0 Hz, Ar-H), 7.32-7.31 (m, 2H, Ar-H), 7.19-7.17 (1H, Ar-H), 6.53-6.51 (2H, Ar-H), 5.47-5.46 (d, 1H, -CH=C in cholesteryl), 4.91-4.87 (1H, m, -CH-O- in cholesteryl), 4.02 (t, 2H,  $J$  = 4.0, 8.0 Hz, -OCH<sub>2</sub>-), 2.58 (s, 3H, Ar-CH<sub>3</sub>), 2.51-2.49 (2H, m, -CH<sub>2</sub> in cholesteryl), 1.08 (s, 3H, -CH<sub>3</sub> in cholesteryl), 0.71 (s, 3H, -CH<sub>3</sub> in cholesteryl), 2.5-0.71 (56 H, m, extensive coupling).

**$^{13}\text{C}$  NMR (100 MHz,  $\text{CDCl}_3$ ,  $\delta$  in ppm):**  $\delta$  = 11.89, 14.14, 15.35, 18.74, 19.39, 21.06, 22.59, 22.69, 22.86, 23.85, 24.31, 26.00, 27.91, 28.04, 28.27, 29.07, 29.25, 29.34, 31.83, 31.88, 31.95, 35.83, 36.20, 36.68, 37.06, 38.21, 39.53, 39.74, 42.34, 50.04, 56.14, 56.70, 68.32, 74.88, 101.52, 107.70, 113.01, 121.38, 122.89, 126.41, 127.55, 132.57, 132.73, 133.59, 139.59, 149.16, 162.34, 163.72, 163.77, 167.57.

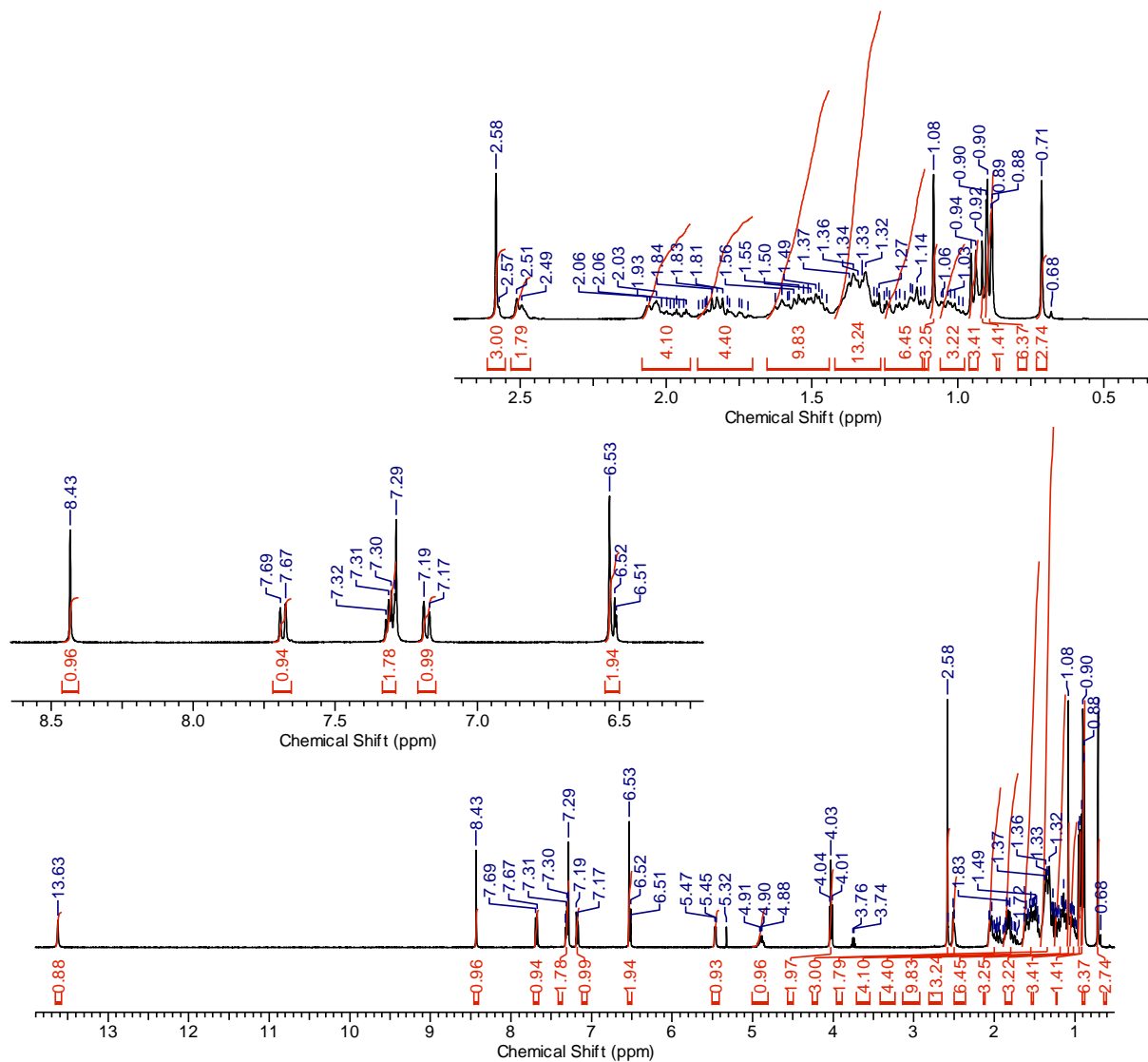


**Figure S8:**  $^1\text{H}$  NMR spectrum of compound 1-8

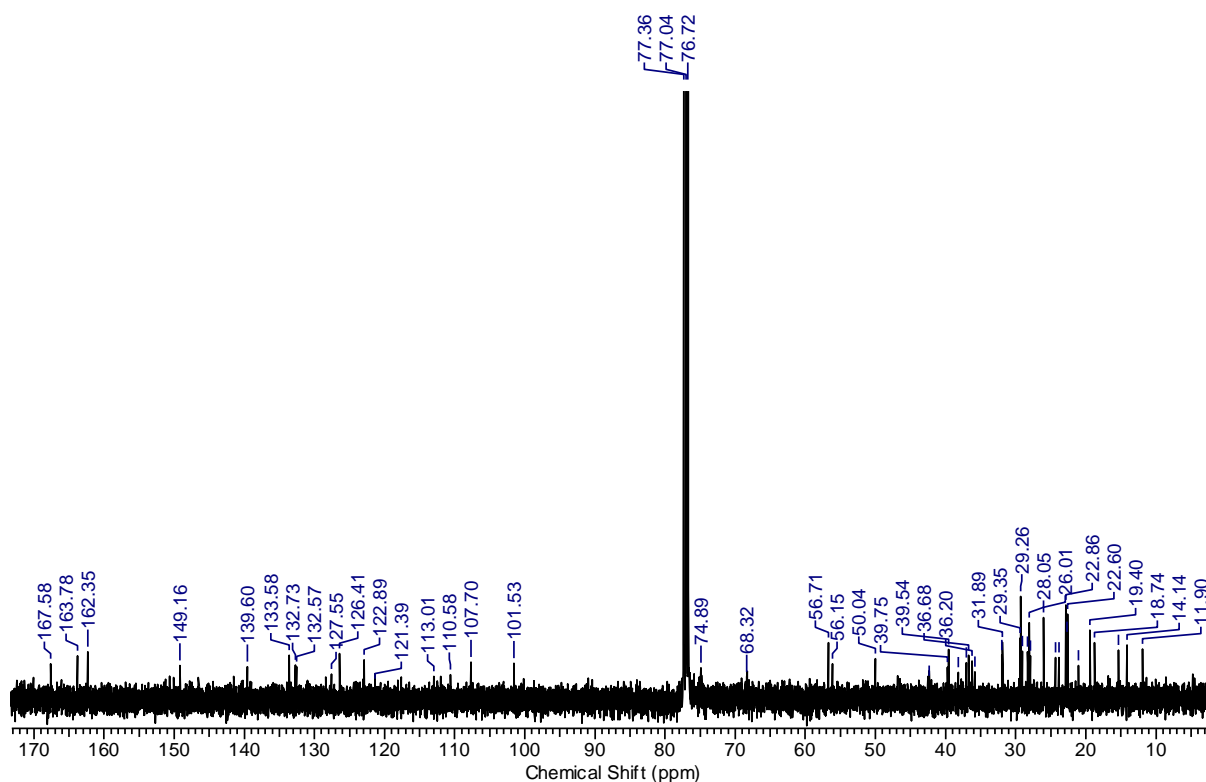


**Figure S9:**  $^{13}\text{C}$  NMR spectrum of compound **1-8**

**Compound 1-16:** Yield = 80%

**FT-IR:** Intramolecular H-bonding of O-H...N at  $3170\text{--}3400\text{ cm}^{-1}$ , C=O stretching band of ester at  $1728\text{ cm}^{-1}$ , HC=N stretching of imine at  $1616\text{ cm}^{-1}$

**UV-vis:** 285.82 nm, 339.22 nm

**$^1\text{H}$  NMR (400 MHz,  $\text{CDCl}_3$ ,  $\delta$  in ppm):**  $\delta$  = 13.62 (s, 1H, -OH), 8.43 (s, 1H, -CH=N), 7.68 (d, 1H,  $J$  = 8.0 Hz, Ar-H), 7.32-7.30 (2H, Ar-H), 7.19-7.17 (1H, Ar-H), 6.53-6.51 (2H, Ar-H), 5.46-5.45 (d, 1H, -CH=C in cholesteryl), 4.93-4.85 (1H, m, -CH-O- in cholesteryl), 4.03 (t, 2H,  $J$  = 8.0, 4.0 Hz, -OCH<sub>2</sub>-), 2.58 (s, 3H, Ar-CH<sub>3</sub>), 2.51-2.48 (2H, m, -CH<sub>2</sub> in cholesteryl), 1.08 (s, 3H, -CH<sub>3</sub> in cholesteryl), 0.71 (s, 3H, -CH<sub>3</sub> in cholesteryl), 2.5-0.71 (m, 74H, extensive coupling).

**$^{13}\text{C}$  NMR (100 MHz,  $\text{CDCl}_3$ ,  $\delta$  in ppm):**  $\delta$  = 11.88, 14.14, 15.33, 18.68, 18.74, 19.38, 21.07, 22.58, 22.71, 22.84, 23.86, 24.31, 25.99, 27.91, 28.03, 28.26, 29.07, 29.38, 29.58, 29.61, 29.68, 29.70, 29.72, 31.89, 31.94, 35.82, 36.20, 36.67, 37.07, 38.22, 39.53, 39.75, 42.33, 50.05, 56.15, 56.70, 68.31, 74.87, 101.53, 107.68, 113, 121.35, 122.87, 126.33, 126.39, 127.49, 127.54, 132.56, 132.74, 133.56, 139.59, 149.13, 149.16, 162.30, 162.33, 163.73, 163.78, 167.56.

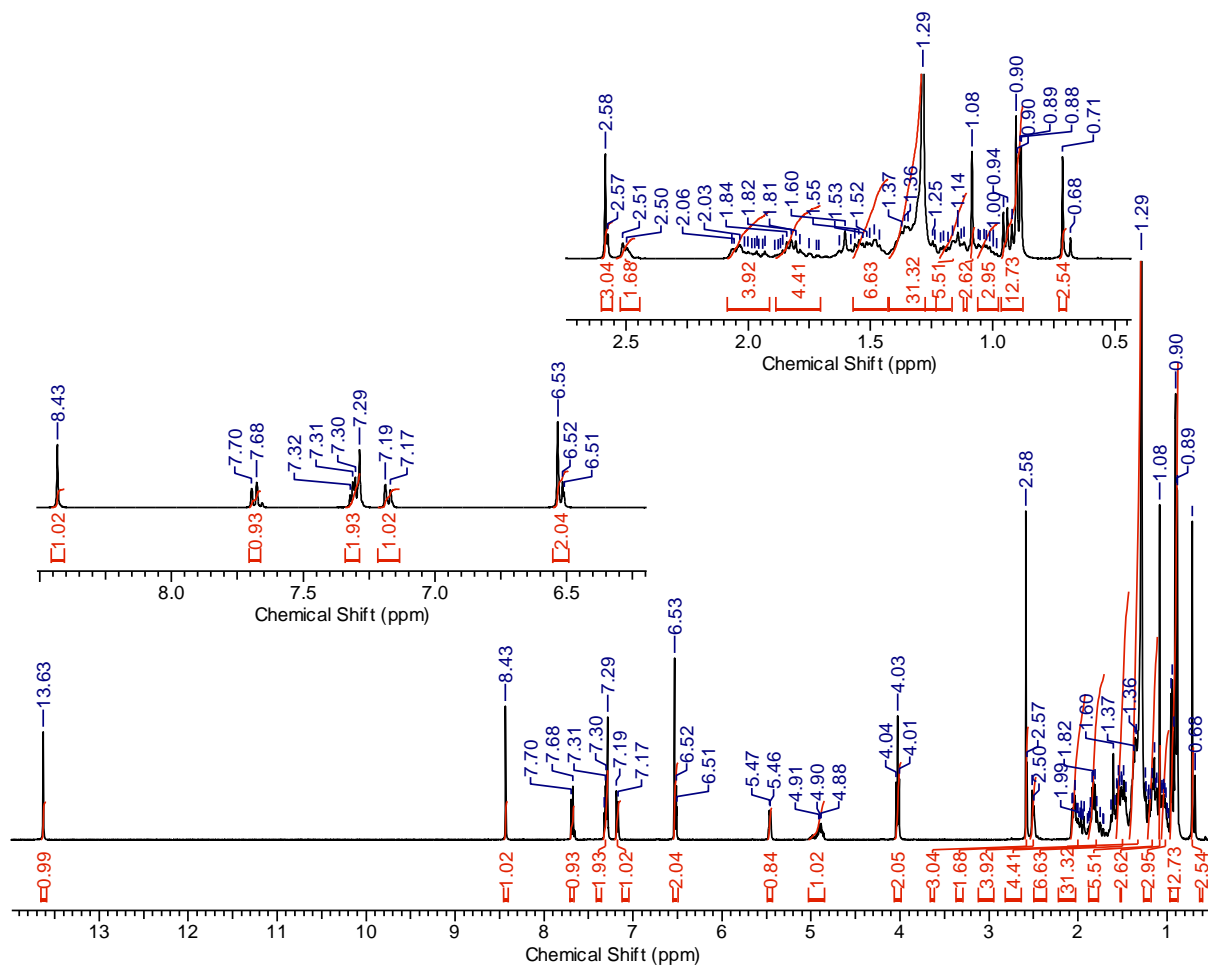
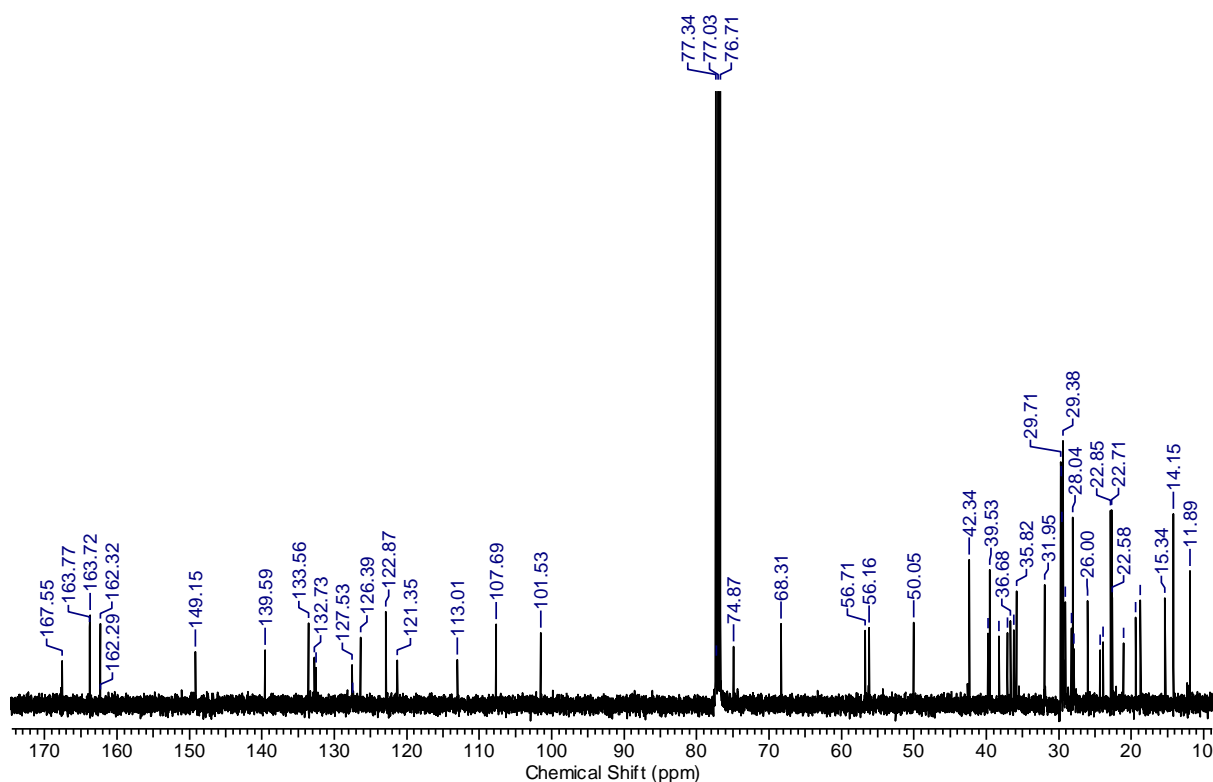


Figure S10:  $^1\text{H}$  NMR spectrum of compound 1-16



**Figure S11:**  $^{13}\text{C}$  NMR spectrum of compound 1-16

**Compound 1-18:** Yield = 85%

**FT-IR:** Intramolecular H-bonding of O-H...N at  $3170\text{--}3400\text{ cm}^{-1}$ , C=O stretching band of ester at  $1728\text{ cm}^{-1}$ , HC=N stretching of imine at  $1616\text{ cm}^{-1}$

**UV-vis:** 285.82 nm, 339.22 nm

**$^1\text{H}$  NMR (400 MHz,  $\text{CDCl}_3$ ,  $\delta$  in ppm):**  $\delta$  = 13.61 (s, 1H, -OH), 8.43 (s, 1H, -CH=N), 7.68 (d, 1H,  $J$  = 8.0 Hz, Ar-H), 7.32-7.30 (2H, Ar-H), 7.19-7.17 (1H, Ar-H), 6.53-6.51 (2H, Ar-H), 5.47-5.45 (d, 1H, -CH=C in cholesteryl), 4.92-4.85 (1H, m, -CH-O- in cholesteryl), 4.03 (t, 2H,  $J$  = 8.0, 4.0 Hz, -OCH<sub>2</sub>-), 2.51-2.48 (2H, m, -CH<sub>2</sub> in cholesteryl), 2.58 (s, 3H, Ar-CH<sub>3</sub>), 1.08 (s, 3H, -CH<sub>3</sub> in cholesteryl), 0.71 (s, 3H, -CH<sub>3</sub> in cholesteryl), 2.5-0.71 (m, 78H, extensive coupling).

**$^{13}\text{C}$  NMR (100 MHz,  $\text{CDCl}_3$ ,  $\delta$  in ppm):**  $\delta$  = 11.86, 11.92, 14.12, 15.42, 18.78, 19.44, 21.06, 22.56, 22.73, 22.89, 23.85, 24.30, 25.99, 27.91, 28.04, 28.27, 28.40, 29.07, 29.39, 29.59, 29.62, 29.68, 29.73, 31.88, 31.95, 32.03, 36.19, 36.67, 37.05, 38.21, 39.53, 39.74, 42.33, 50.03, 56.16, 56.70, 68.31, 74.84, 74.92, 101.55, 107.64, 112.99, 121.36, 122.82, 122.95, 122.99, 126.31, 126.42, 127.54, 132.57, 132.71, 133.54, 133.61, 139.58, 149.15, 162.28, 162.38, 163.72, 163.77, 167.58.



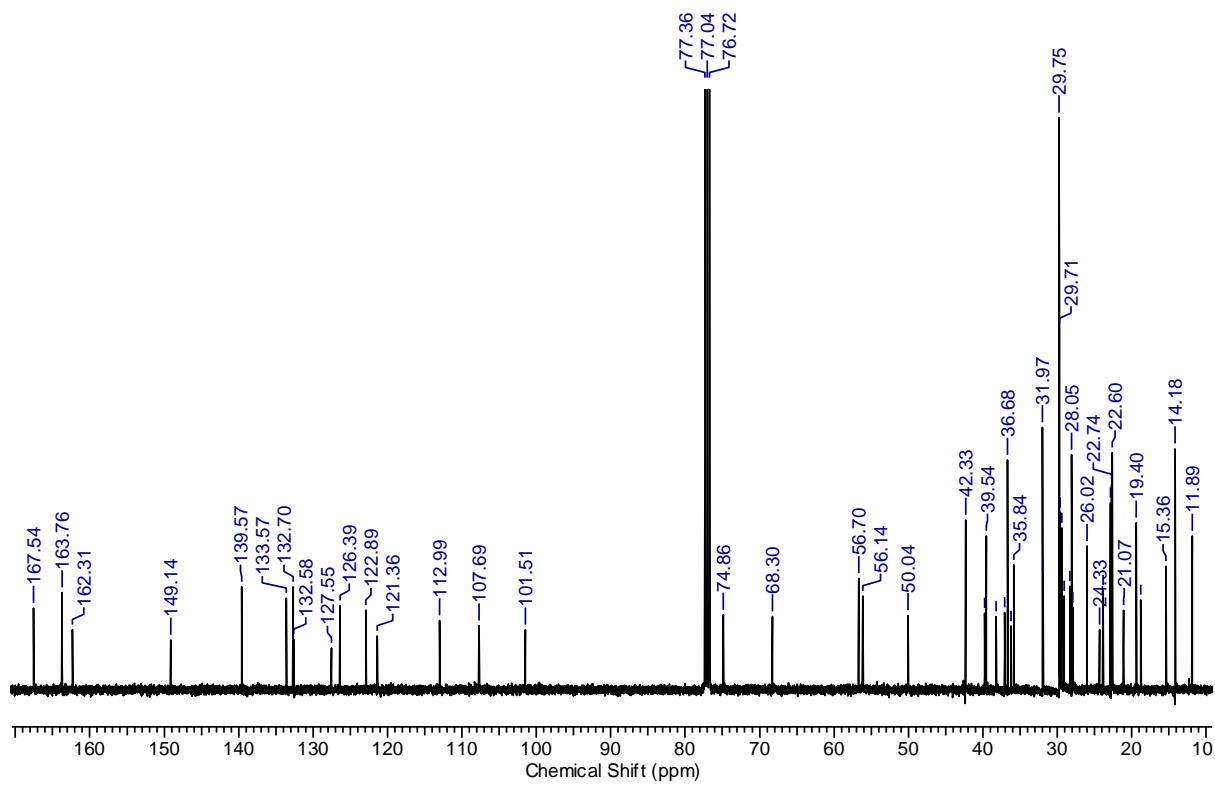
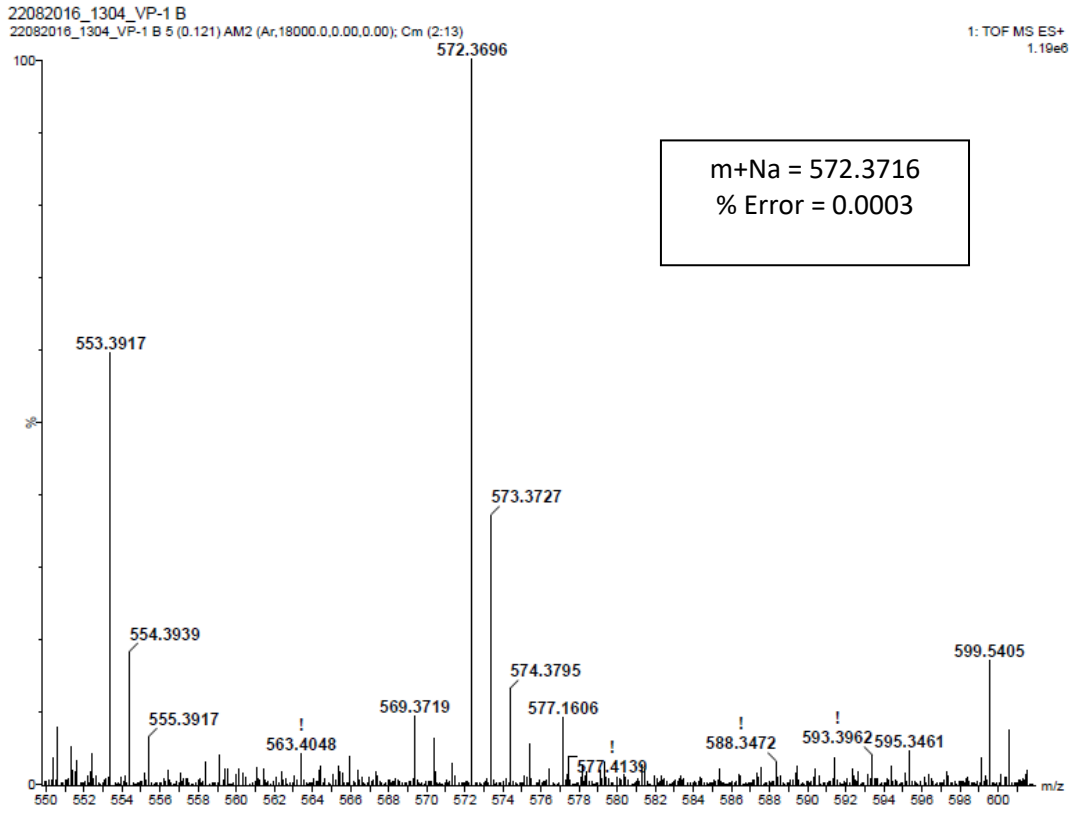


Figure S13:  $^{13}\text{C}$  NMR spectrum of compound 1-18

**Electrospray Ionisation Mass Spectroscopy:**



Figure

S14: ESI spectrum of compound f

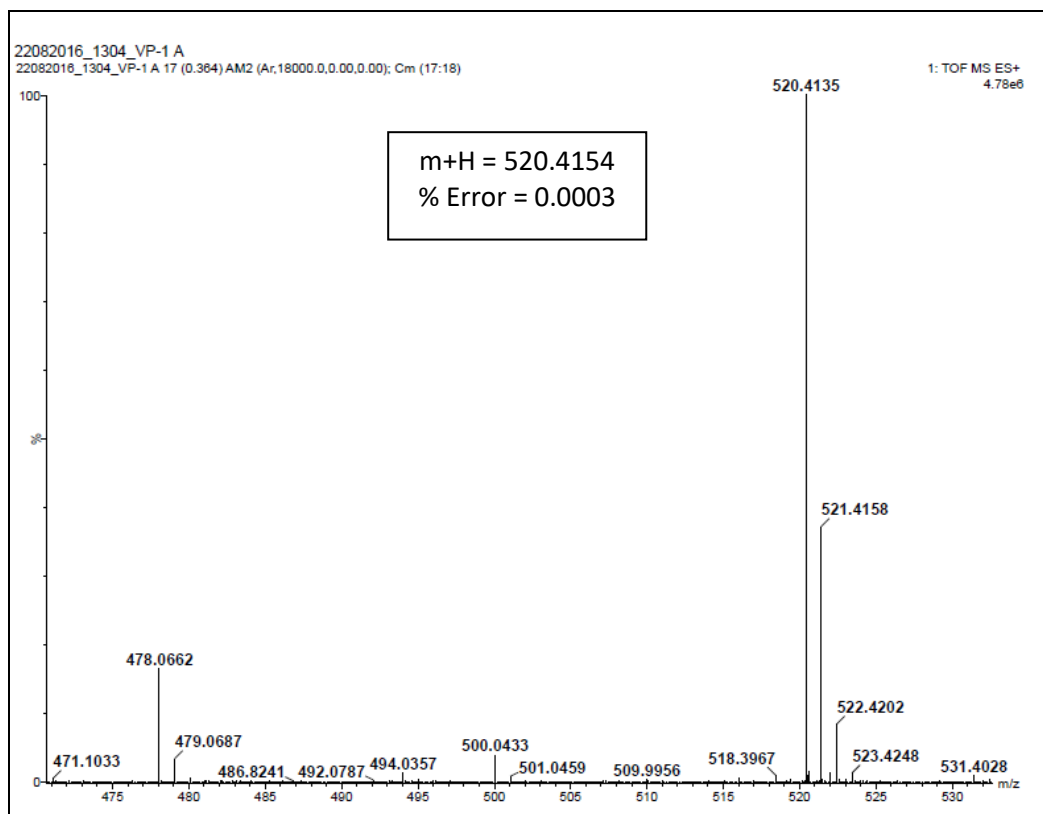


**Figure S15:** ESI spectrum of compound **g**

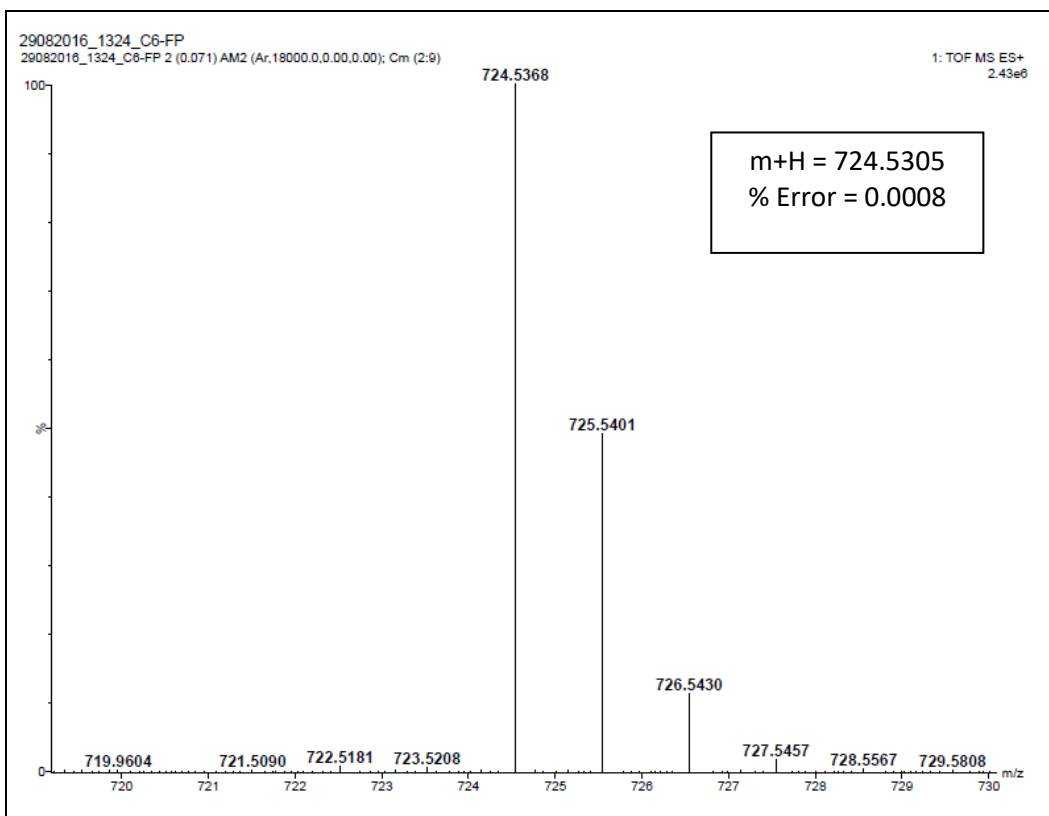


**Figure S16:** ESI spectrum of compound **1-6**

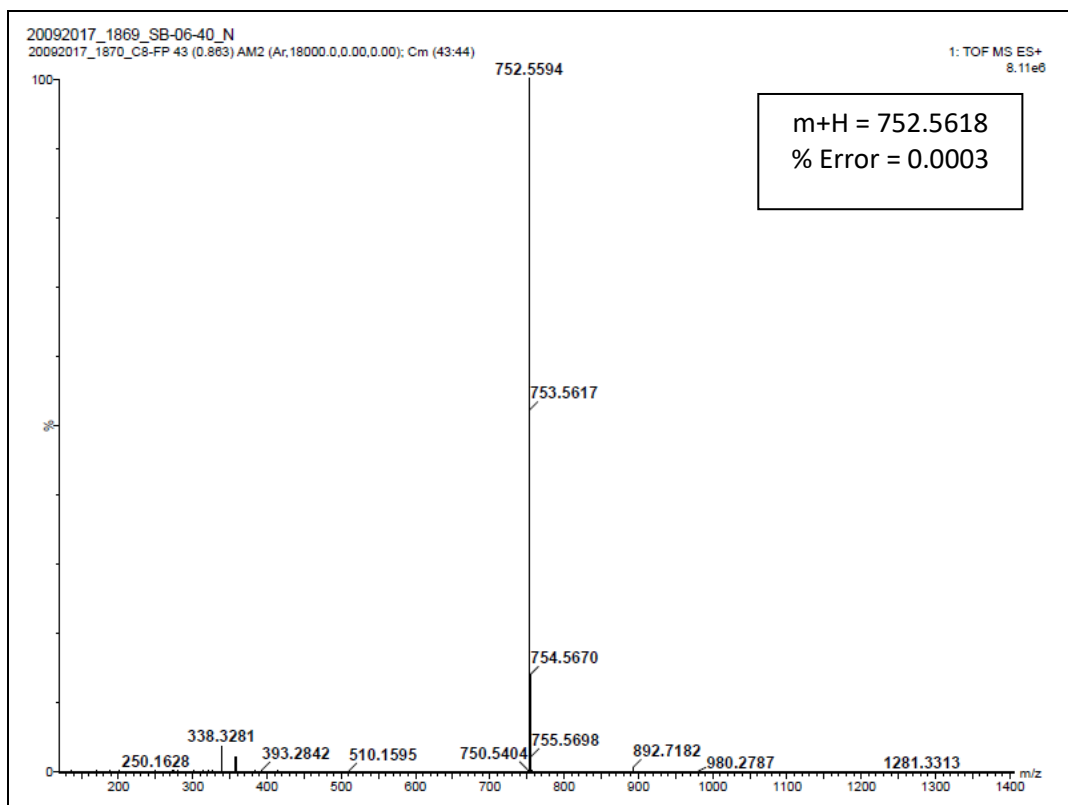


**Figure S17:** ESI spectrum of compound **1-8**

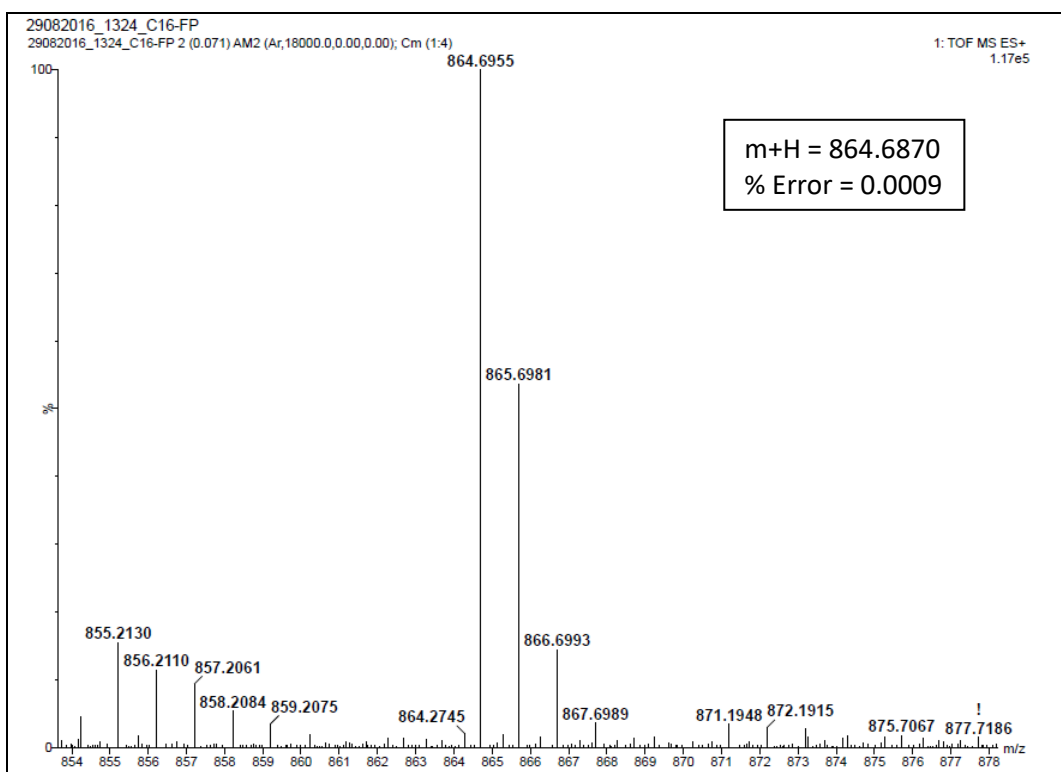


**Figure S18:** ESI spectrum of compound **1-16**

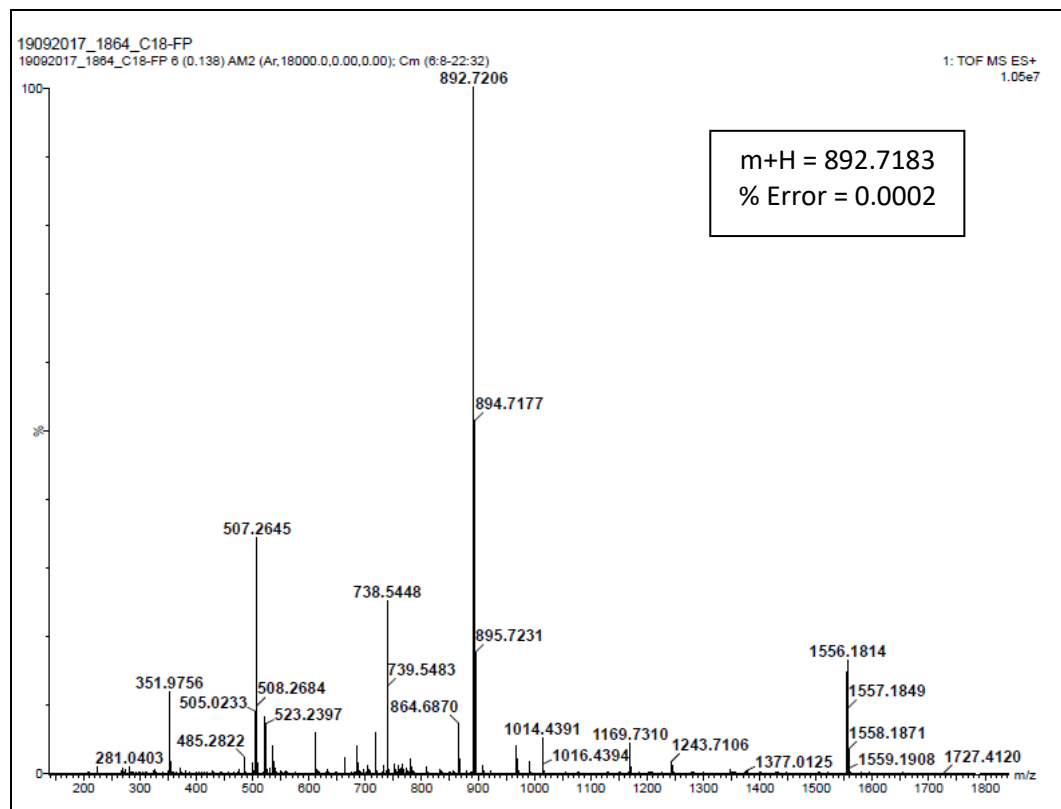


**Figure S19:** ESI spectrum of compound **1-18**

### 3. UV-Visible studies:

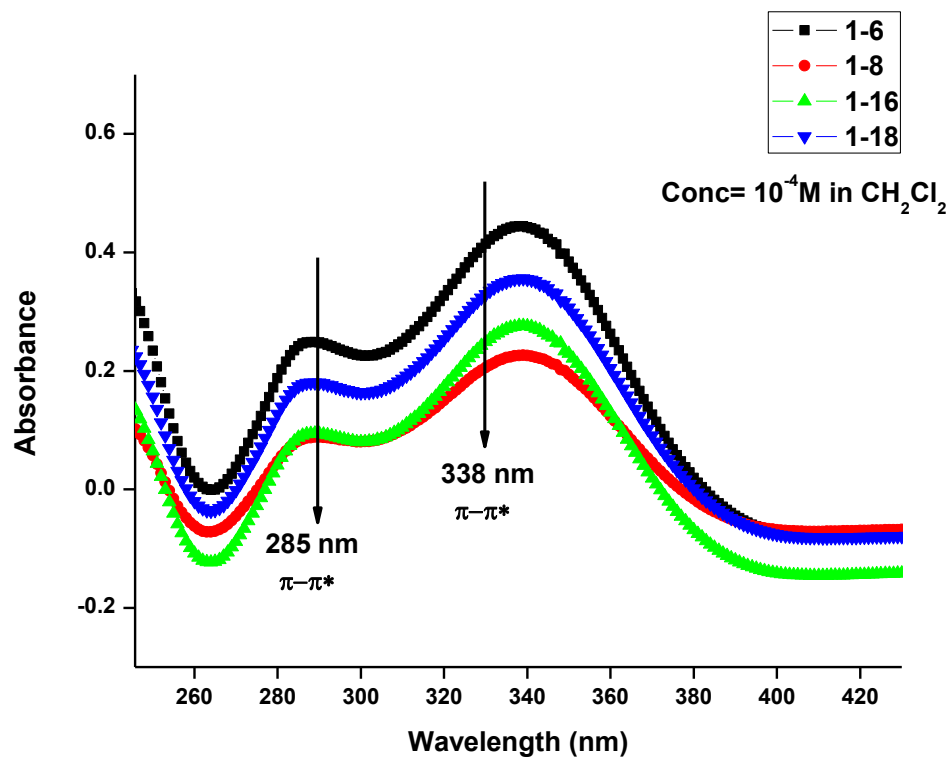
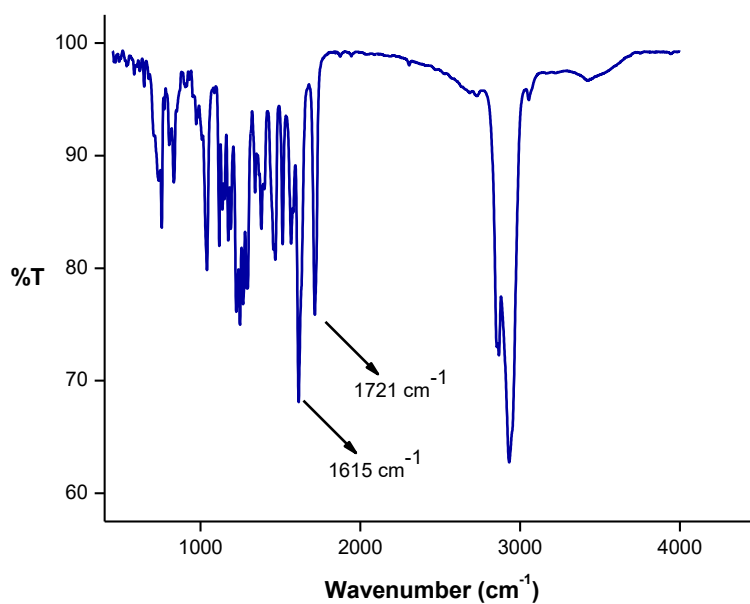


Figure S20: UV-Vis spectrum of 1-n series

### 4. IR studies:



**Figure S21:** IR spectrum of compound **1-8**

## 5. Polarising Optical Microscopy:

### Optical Micrographs of 1-6:

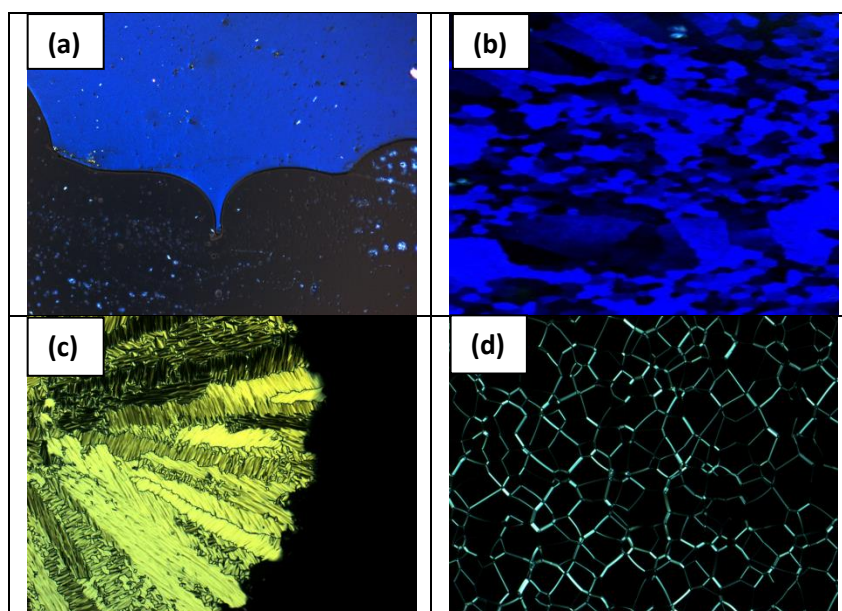


**Figure S22:** POM micrographs of **1-6** (a) BPIII at 180.4 °C (b) BPI/BPII at 179.5 °C (on cooling, Magnification 10X) (c) N<sub>cyb</sub>\* at 178.5 °C (d) N<sub>cyb</sub>\* at 155 °C (on heating, Magnification 20X)

Blue Phases (BPs), classified into three categories, namely, a body-centered-cubic BP (BPI), simple cubic BP (BPII) and amorphous BP (BPIII) in order of increasing transition temperature.

### Optical Micrographs of 1-16:

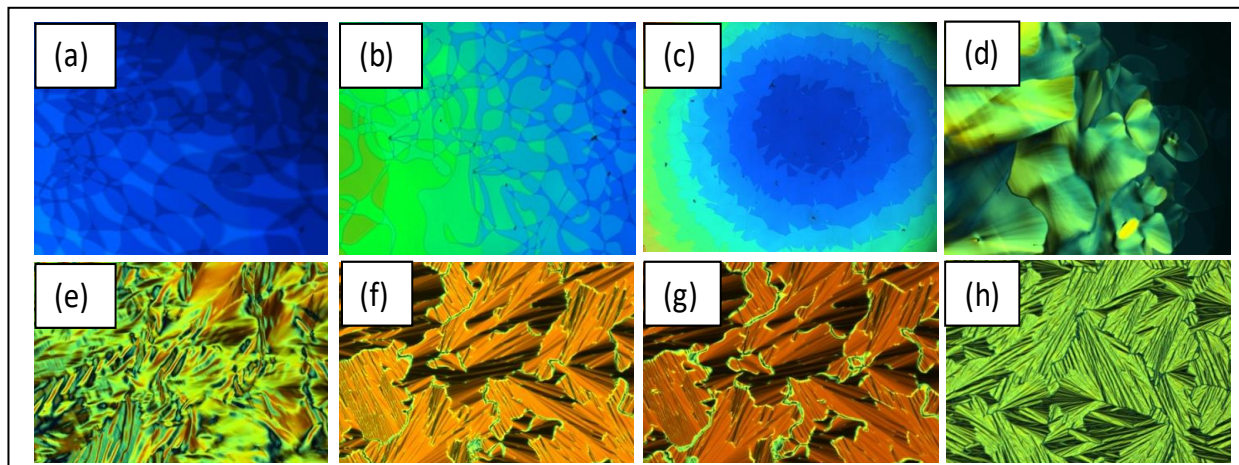


**Figure S23:** POM micrographs of **1-16** (a)  $N_{cyb}^*$  at 147.8 °C (b)  $N_{cyb}^*$  at 147.0 °C (c)  $N_{cyb}^*$  at 146.8 °C (d) TGBA at 142.5 °C (e) TGBA at 125 °C (f) SmA at 105.3 °C (g) SmA at 92.5 °C (h) SmX at 82.2 °C. All the POM textures were recorded on cooling at the rate of 10°C/min under crossed polarisers 10X. All these POM micrographs were captured in **planar cell** of **4.8  $\mu\text{m}$**  thickness.

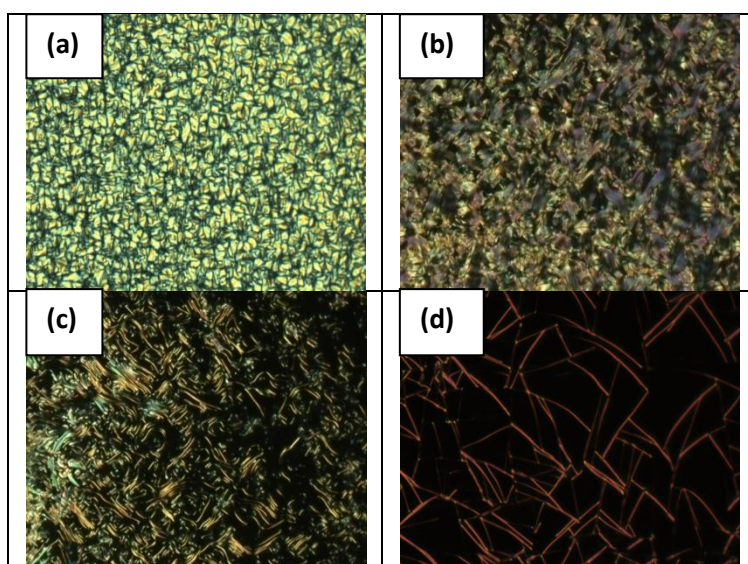


**Figure S24:** POM micrographs of **1-16** (a)  $N_{cyb}^*$  at 146.5 °C (b) TGBA at 139 °C (c) TGBA at 138 °C (d) TGBA at 141 °C (on heating). All these POM textures were captured in an **untreated glass cell** separated by a myler spacer of thickness **2.5 $\mu\text{m}$** . (Magnification 10X, crossed polarizers)

In general, the filamentous texture is obtained when the sample is placed in a homeotropic cell but the compound **1-16** and **1-18** shows these filamentous textures in an untreated glass

cell. These compounds **1-16** and **1-18** have the tendency to align homeotropically. These filamentous textures are significant of TGBA phase.

**POM micrographs of 1-18:**

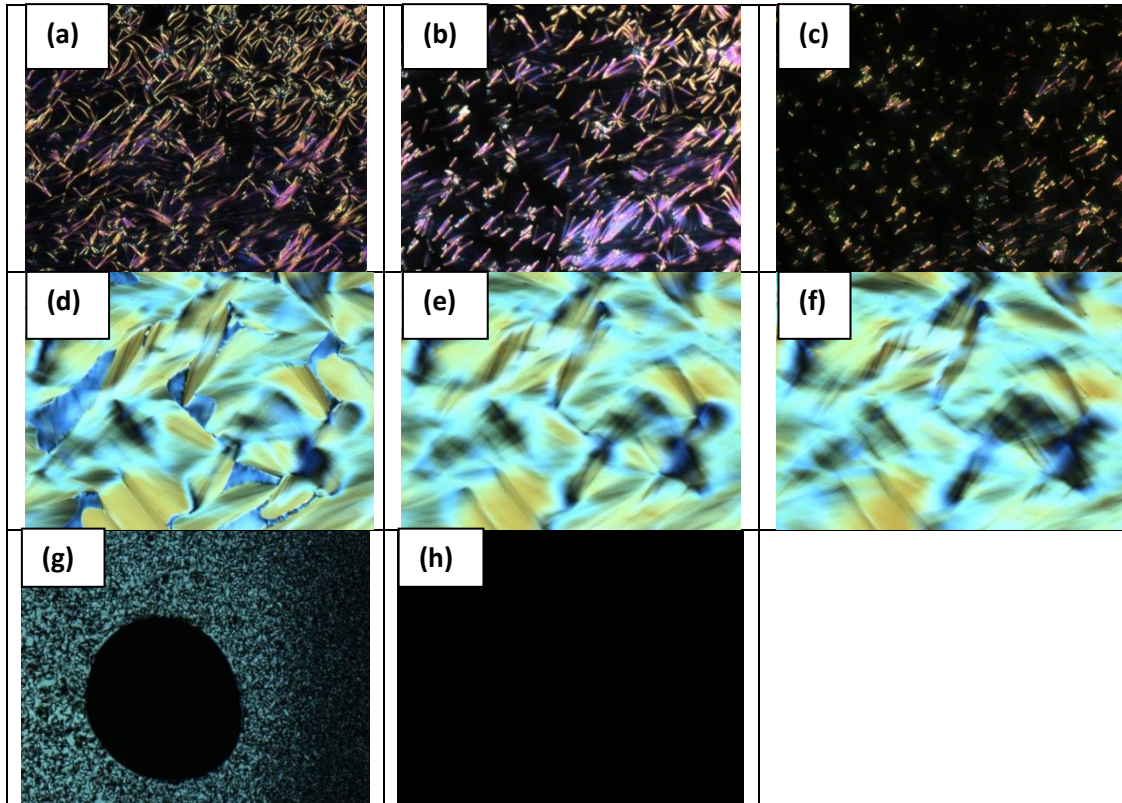


**Figure S25:** POM micrographs of **1-18** (a) TGBA at 141.0°C (b) TGBA at 140.5 °C (c) TGBA at 139 °C (d) TGBA at 138.3 °C (e) TGBA at 137 °C (f) TGBA at 134.6 °C (g) Focal conic texture of N<sub>cyb</sub>\* at 143.0 °C (h) Homeotropic texture at 130.5 °C. These textures were recorded on cooling.

POM textures a,b,c were captured in an **untreated glass cell** separated by a myler spacer of thickness **2.5 μm**.

POM textures d,e,f were taken in an **ITO coated with planar alignment** with cell gap **4.8 μm**.

POM textures g,h were recorded in a an **ITO coated cell with homeotropic alignment** of thickness **3.3 μm**.

## 6. Differential Scanning Calorimetry:

**Table S1.** Phase transition temperatures (peak temperature, °C) and enthalpies of transition ( $\Delta H$ , kJ mol<sup>-1</sup>, in parentheses) determined by DSC (scan rate 10 °C min<sup>-1</sup>) and by POM.

Comp	Phase transitions
<b>1-6</b>	<b>Heating:</b> Cr 154.7 [25.33] N <sub>cyb</sub> * 181.2 [0.21] Iso <b>Cooling:</b> Iso (181.0 BPIII 180.3 BPII/I) <sup>a</sup> 178.9 [0.34] N <sub>cyb</sub> * 81.9 [13.3] Cr
<b>1-16</b>	<b>Heating:</b> Cr 125.3 [29.3] TGBA 143.5 [0.43] N <sub>cyb</sub> * 150.0 [0.19] Iso <b>Cooling:</b> Iso 148.9 [0.33] N <sub>cyb</sub> * 142.3 [0.54] TGBA 110.6 (SmA 92.2) <sup>a</sup> SmX 88.3 [17.5] Cr

<sup>a</sup>Round brackets for monotropic phases; abbreviations: Cr = crystal; Iso = isotropic; N<sub>cyb</sub>\* = chiral nematic phase composed of Sm clusters; SmA<sub>P</sub> = orthogonal smectic structure with layer polarization antiparallel; TGBA = twisted grain boundary phase; for DSC thermograms

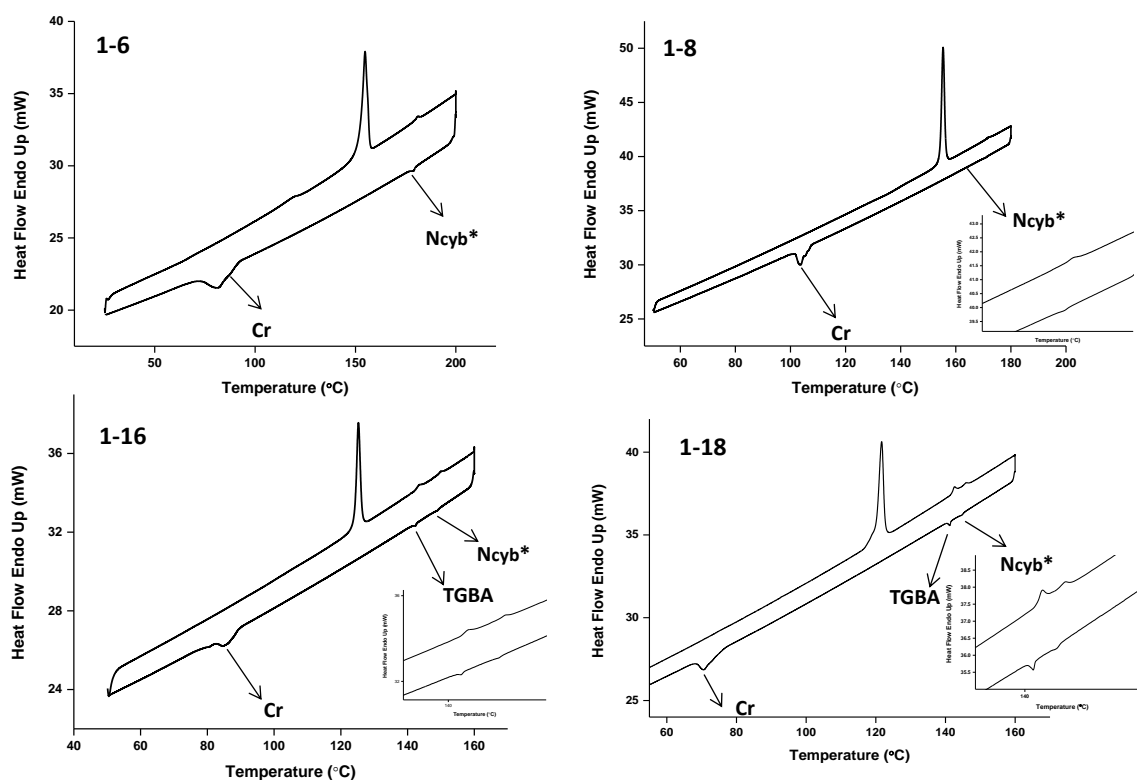


**Figure S26:** DSC thermograms of **1-6**, **1-8**, **1-16** and **1-18**

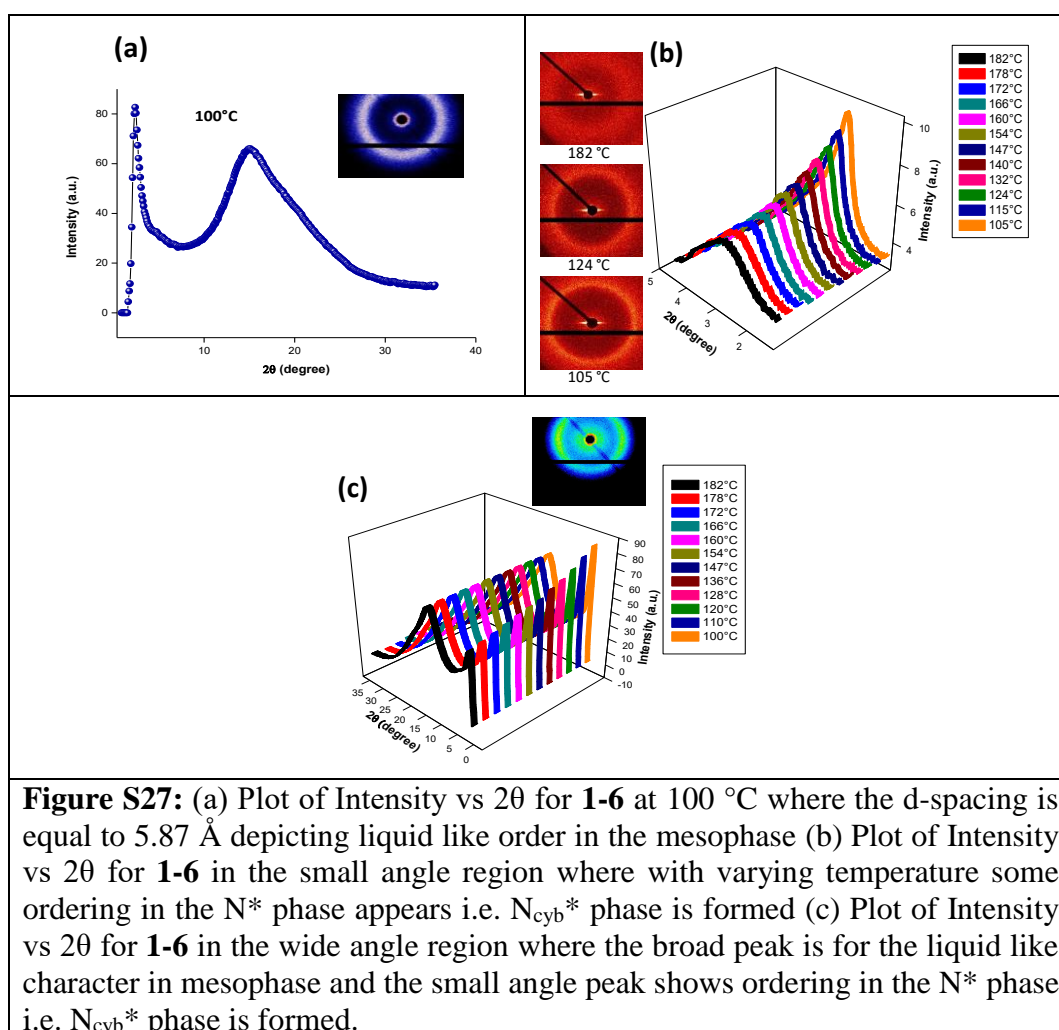
**1-6** and **1-8** exhibit only one mesophase i.e. N<sub>cyb</sub>\* whereas **1-16** and **1-18** exhibit four mesophases. However we are able to distinguish only two mesophases in the DSC thermogram whereas the other two mesophases i.e (SmA and SmX) in **1-16** and **1-18** does not show measurable enthalpy change as seen in Figure S25. This indicates that major structural transformations take place at the Iso–N transition and N to TGBA. It appears that

the other phase transitions are continuous and mainly associated with the growth of the cybotactic clusters and twisting of these cybotactic clusters.

## 7. Temperature dependent X-ray diffraction studies:

Detailed X-ray diffraction (XRD) measurements were carried out to investigate the phase structure for all the four compounds at a slow cooling rate from the isotropic liquid.

### XRD Data of 1-6:



**XRD Data of 1-18:**

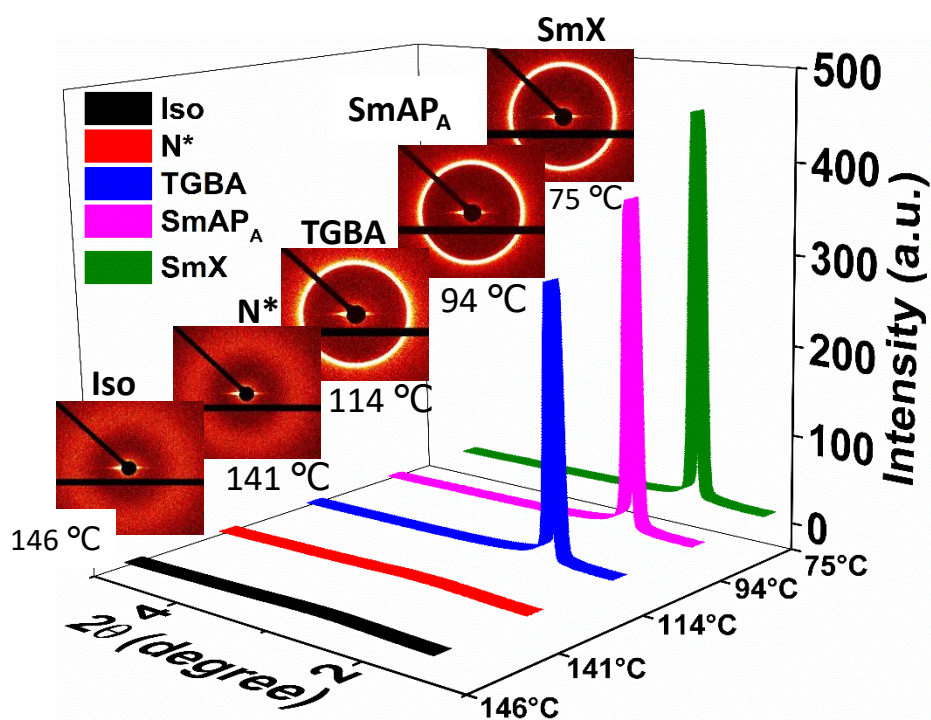


**Figure S28:** Comparative plot of intensity vs  $2\theta$  in small angle region at different temperatures with 2D-diffraction images in the mesophase range of compound **1-18**

**Table S2:** Variation of d spacing with temperature in the entire mesophase range of **1-18**

Temperature (°C)	d-value/Å	Molecular length/Å
145	37.50	50.55
143	37.65	
141	37.65	
139	38.56	
137	39.50	
135	40.36	
134	42.14	
133	44.04	
132	44.78	
131	45.37	
129	46.57	
126	47.34	
123	47.69	
120	47.77	
117	47.77	
114	47.77	
110	47.99	
107	48.05	
104	48.22	

100	48.22	
97	47.74	
94	47.28	
90	46.83	
87	46.82	
84	46.42	
80	45.96	
79	45.94	
77	45.50	
75	45.48	

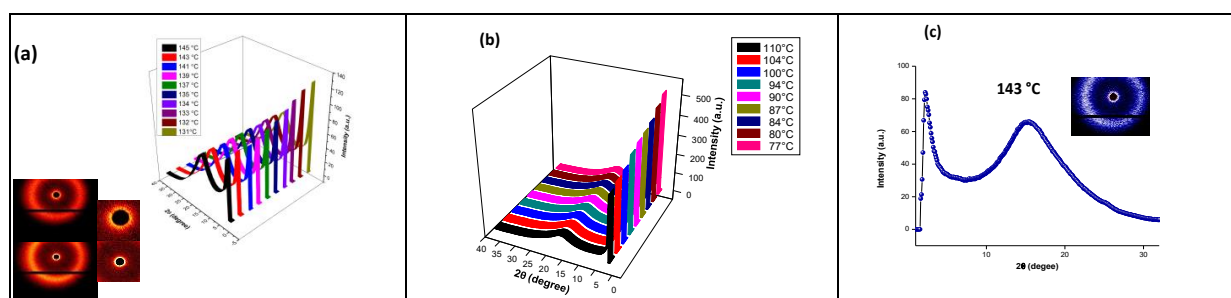


**Figure S29:** (a) Plot of Intensity vs  $2\theta$  as the compound **1-18** makes a transition from  $N_{cyb}^*$  to TGBA (Left hand side of the figure shows the 2D diffraction plots of **1-18** in the Nematic phase as well as the TGBA phase. The upper figure shows a diffuse peak in the small angle region signifying  $N_{cyb}^*$  whereas the lower figure shows a sharp peak in the small angle region signifying TGBA) (b) Plot of Intensity vs  $2\theta$  as **1-18** transits from  $SmAP_A$  to  $SmX$  (c) Plot of Intensity vs  $2\theta$  for **1-18** at  $143^\circ\text{C}$  in the  $N_{cyb}^*$  phase.

### XRD Data of 1-16:

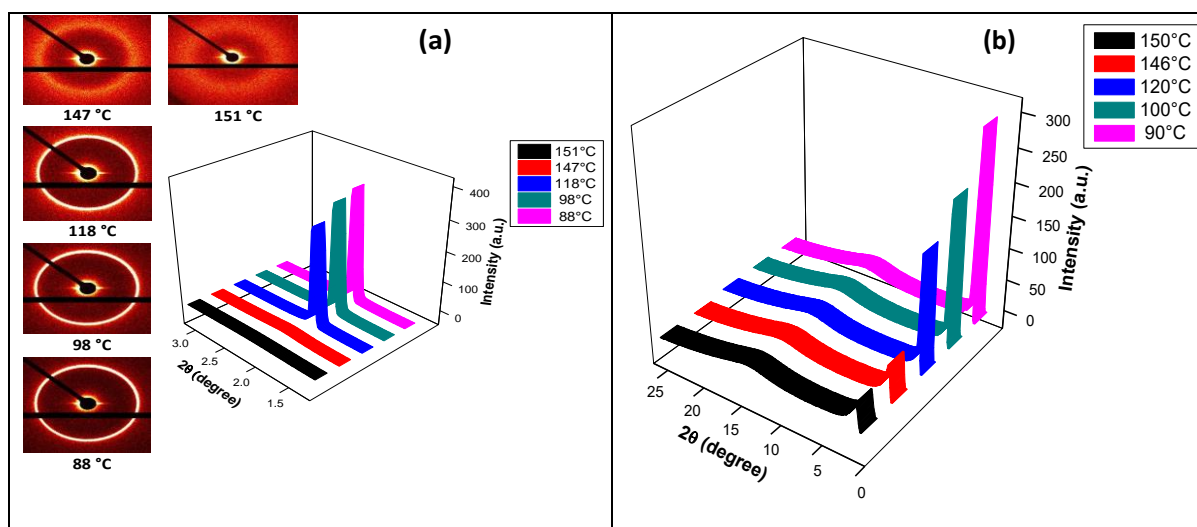


**Figure S30:** (a) Plot of Intensity vs  $2\theta$  for **1-16** in the small angle region as the temperature is decreased showing four different mesophases i.e.  $N_{cyb}^*$ , TGBA, SmA and SmX (b) Plot of Intensity vs  $2\theta$  for **1-16** in the wide angle region showing an increase of intensity in the small angle region as the temperature is decrease for the four different mesophase i.e.  $N_{cyb}^*$ , TGBA, SmA and SmX

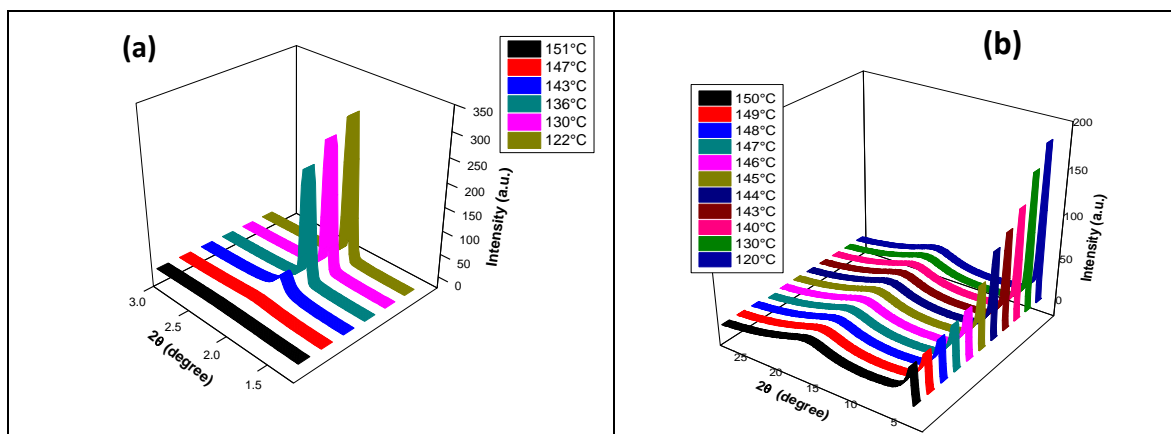


**Figure S31:** (a) Plot of Intensity vs  $2\theta$  for **1-16** as the compound makes a transition from  $N^*$  to TGBA in the small angle region (b) Plot of Intensity vs  $2\theta$  for **1-16** where the broad peak in the wide angle region is due to liquid-like character in the mesophase whereas the continuous increase in the intensity of the small angle region can be attributed to the change in the mesomorphic characteristics i.e. **1-16** makes a transition from  $N^*$  to TGBA

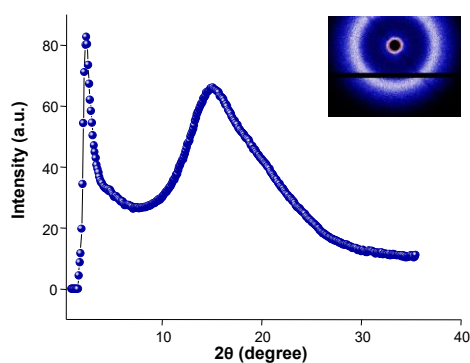


**Figure S32:** Plot of Intensity vs  $2\theta$  for **1-16** at 147 °C

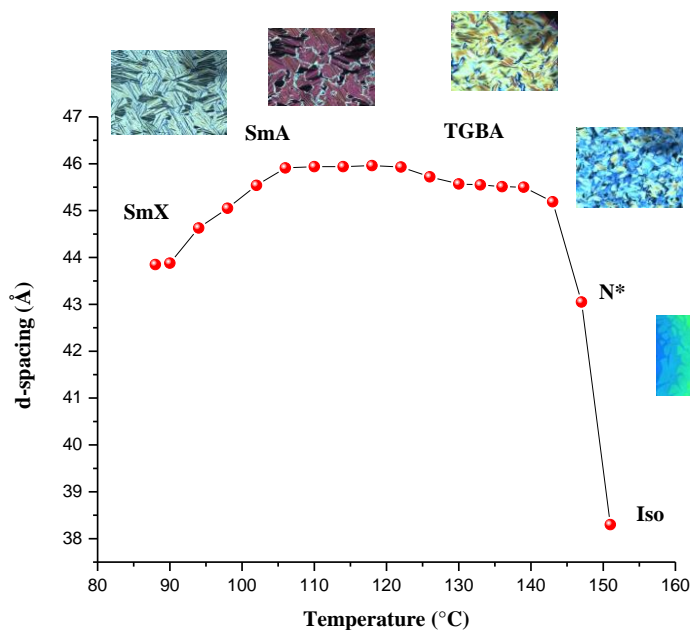


**Figure S33:** Variation of  $d$ -spacing as the temperature is varied in **1-16**

The  $d$ -value gradually increase upon decreasing the temperature until TGBA structure transform to SmA phase ( $d/L = 0.95$ ) which upon further cooling transform to another unidentified tilted SmX phase with decrease in  $d$ -value which continues until 88 °C.

**Correlation Length:** The correlation length is the degree of order of the LC molecules in the mesophases which can be calculated by Scherrer Equation.

$$\xi = K\lambda / \Delta 2\theta \cos\theta$$

where  $\xi$  is the correlation length,  $K$  is the shape factor whose value is equivalent to unity,  $\Delta 2\theta$  is the line broadening at full width half maxima (FWHM) in radian unit and  $\theta$  is the maxima of the reflection.

The correlation value was calculated for both **1-6** and **1-8** which shows that the value of the correlation length increases with decrease in temperature and clearly illustrates that there is increase in the ordering within the mesophases i.e.  $N_{cyb}^*$  phase is formed.

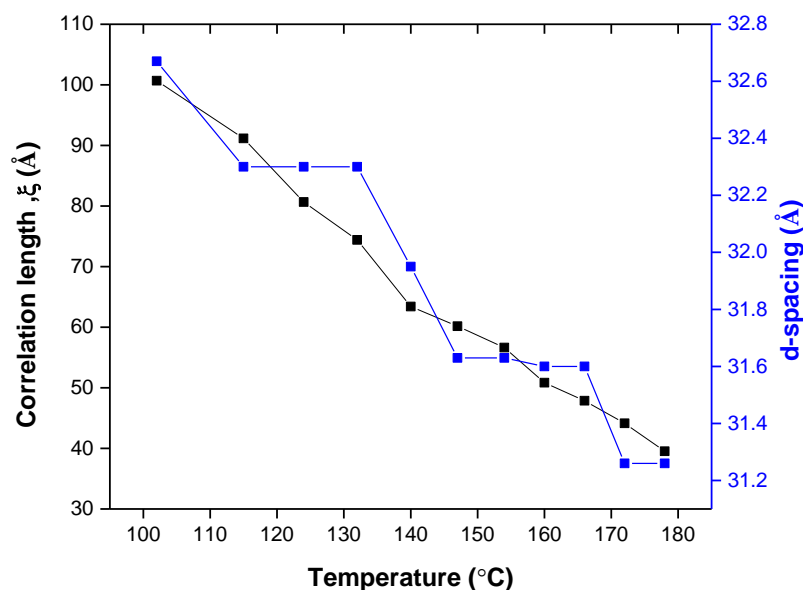


**Figure S34:** Plot of Correlation Length and d-spacing vs Temperature for **1-6** shows an increase in the correlation length as well as d spacing as the temperature is decreased.

## 8. Thermochromism:

Thermochromism is the ability of the material to change the colours as the temperature is varied due to selective reflection of the light when visible light falls on liquid crystals ( $\lambda = np$ , where  $p$  is the pitch length of the helical structure and  $n$  is the average refraction index of the LC material)..

Cholesteric Liquid Crystals (CLCs) are widely considered as thermochromic materials due to their Bragg's type scattering of the incident light that found various device applications. In general, thermotropic CLCs are viewed against a black background because the selective reflection caused by CLCs can be effectively seen by it. However if the liquid crystal is viewed against a white background the background between them reflects all the wavelength of colours and hence the colour is lost. We have also carried out all the experiments against a dark black surface.

Thermotropic liquid crystals exploit two main phase transitions in the design of thermochromic devices:

Iso to N\* which gives a particular colour and can be used in those devices which require one colour whereas N\* to SmA can be used in those device which require a series of colour change i.e. from blue to red.

The pitch of the CLCs can be fixed in the glassy state by quenching, to form solid coloured films. N. Tamaoki et al have published a lot of articles on the colour recording of dicholesteryl esters with molecular weights over 1000 which can be solidified, maintaining cholesteric colors between two glass plates.

We have shown in the main paper thermochromism in **1-6** which exhibit  $N_{cyb}^*$  phase. Therefore, the yellow colour of the isotropic liquid changes to blue colour as the liquid crystal is cooled which further changes to green and then crystallises. This method to capture a coloured cholesteric solid film can be used for rewritable full colour recording. We have also tried to obtain the blue colored cholesteric solid film by vitrifying the thin film in ice bath. Therefore, these cholesteric films can be considered to be a good candidate for the full colour recording.

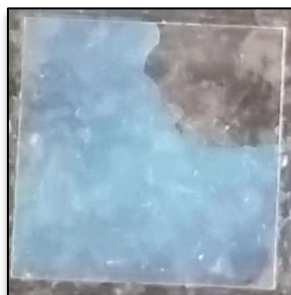


**Figure S35:** Vitrified image of **1-6** after dipping the glass slide in ice cold bath

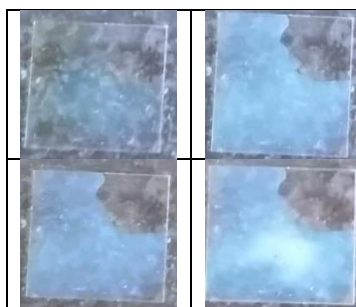


**Figure S36:** Thermochromism in **1-6**

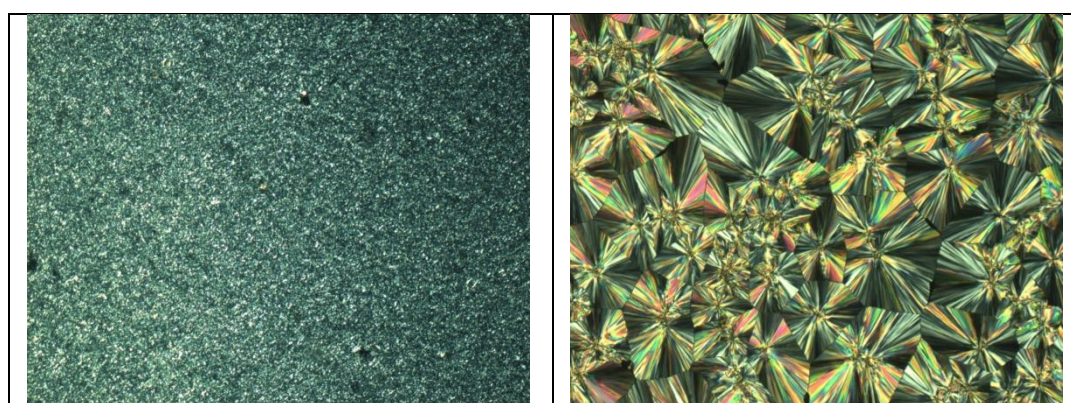


**Figure S37:** POM micrographs of vitrified sample **1-6** (a) at room temperature (b) at 82.3 °C. All the images were recorded at the cooling rate of 10 °C/min under 10X crossed polarisers.

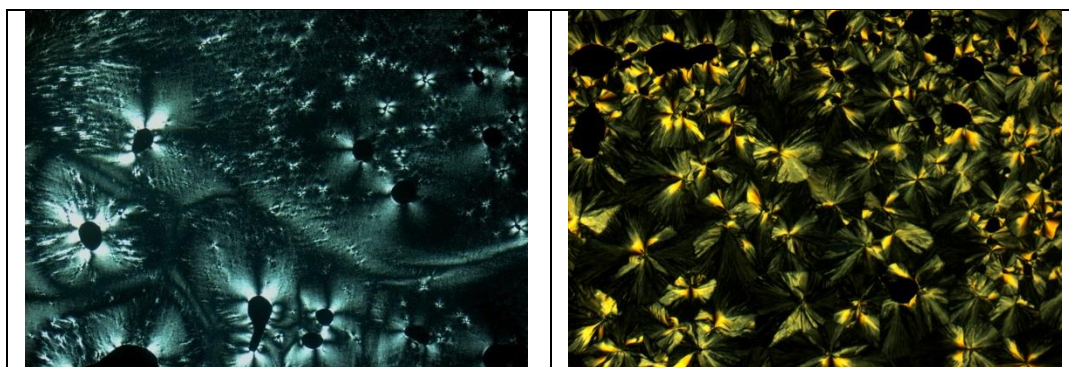


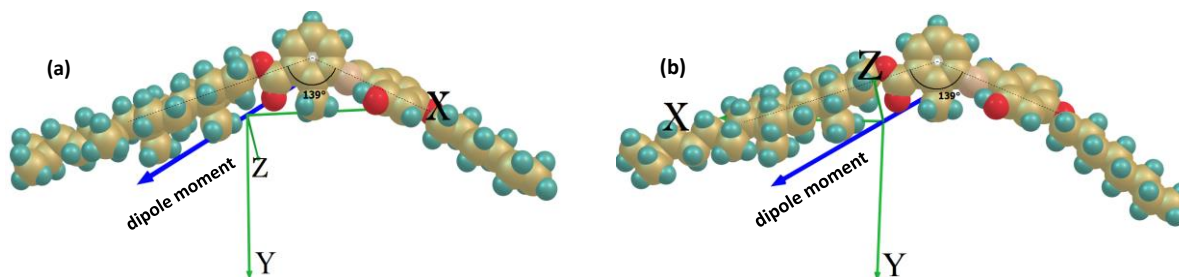
**Figure S38:** POM micrographs of vitrified sample **1-8** (a) at room temperature (b) at 84.5°C. All the images were recorded at the cooling rate of 10 °C/min under 10X crossed polarisers.

**1-6** and **1-8** on quenching form a glassy state whose POM textures have been shown above. These POM textures do not show any sign of crystallisation at room temperature. However, on heating it gets converted into the crystalline state at 82.3 °C in **1-6** and 84.5 °C in **1-8**.

### 9. Details of DFT calculations:

Quantum chemical calculation based on density functional theory (DFT) has been performed in order to focus on the spatial geometry/shape of the molecules. Geometry optimizations have been carried out without imposing any constraints using the Gaussian 09 program package through DFT calculation. For all the calculations 6-311g (d, p) basis set with B3LYP exchange-correlation functional has been used.

For all the compounds, the calculated torsional angles between the central phenyl ring and adjacent phenyl rings are in the range of ~130° (as shown in Figure S37) which designate the non-co-planarity in shape and flexibility around the linking groups. The extended bent angle (~139°-143°) calculated for all the four compounds signify that these types of molecules are in the borderline between calamitic and bent-core mesogens which also support the possibility of existence of local molecular ordering in the nematic phase ( $N_{cyb}$ ). All the dipole moment components and resultant dipole moment obtained from the optimized geometry are depicted in Table S2.



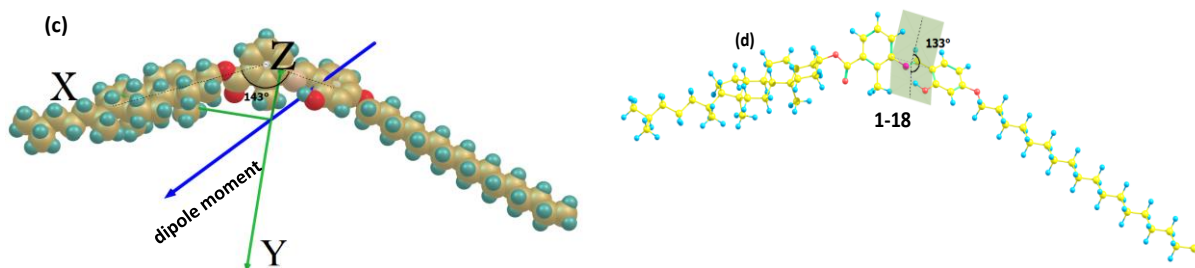


**Figure S39:** Optimized geometry showing bent angle and resultant dipole moment direction (a) **1-6**; (b) **1-8**; (c) **1-16** and (d) torsion angle of **1-18**.

**Table S3:** DFT calculated bend angle  $\theta$ , dipole moment components ( $\mu_x$ ,  $\mu_y$ ,  $\mu_z$ ), the resultant dipole moment ( $\mu$ ) and molecular length.

Compounds	Dipole moment (Debye)				Bend angle ( $^\circ$ ) $\theta$	Molecular length ( $\text{\AA}$ )
	$\mu_x$	$\mu_y$	$\mu_z$	$\mu_{\text{resultant}} = (\mu_x^2 + \mu_y^2 + \mu_z^2)^{1/2}$		
1-6	1.22	0.87	0.37	1.55	139	35.9
1-8	1.18	0.84	0.30	1.48	139	37.9
1-16	1.09	0.84	0.17	1.59	143	47.9
1-18	1.02	1.19	0.15	1.58	143	50.5

The values relative to angles and dipole moment are expressed in degree ( $^\circ$ ) and Debye (D) respectively.

The calculation of atomic orbital composition, namely HOMO and LUMO, provides the important information related to different physical properties which help for the design of new molecules and tuning of distinct desired properties of the compounds. The HOMO–LUMO energy separation is measured of kinetic stability of the molecule and could indicate the reactivity pattern. A large HOMO–LUMO energy gap indicates high kinetic stability and low chemical reactivity, because it is energetically unfavourable to add electrons to a high-lying LUMO or to extract electrons from a low-lying HOMO. The HOMO–LUMO energy gaps for all the compounds is 4.17 eV, and imply that the compounds are fairly stable (Figure S38). Further, the electron density of the molecular orbitals, that is, HOMO and LUMO of all the compounds are mainly concentrated in the aromatic region of the molecules. Dipole moment for all the compounds have been calculated along the three Cartesian directions.

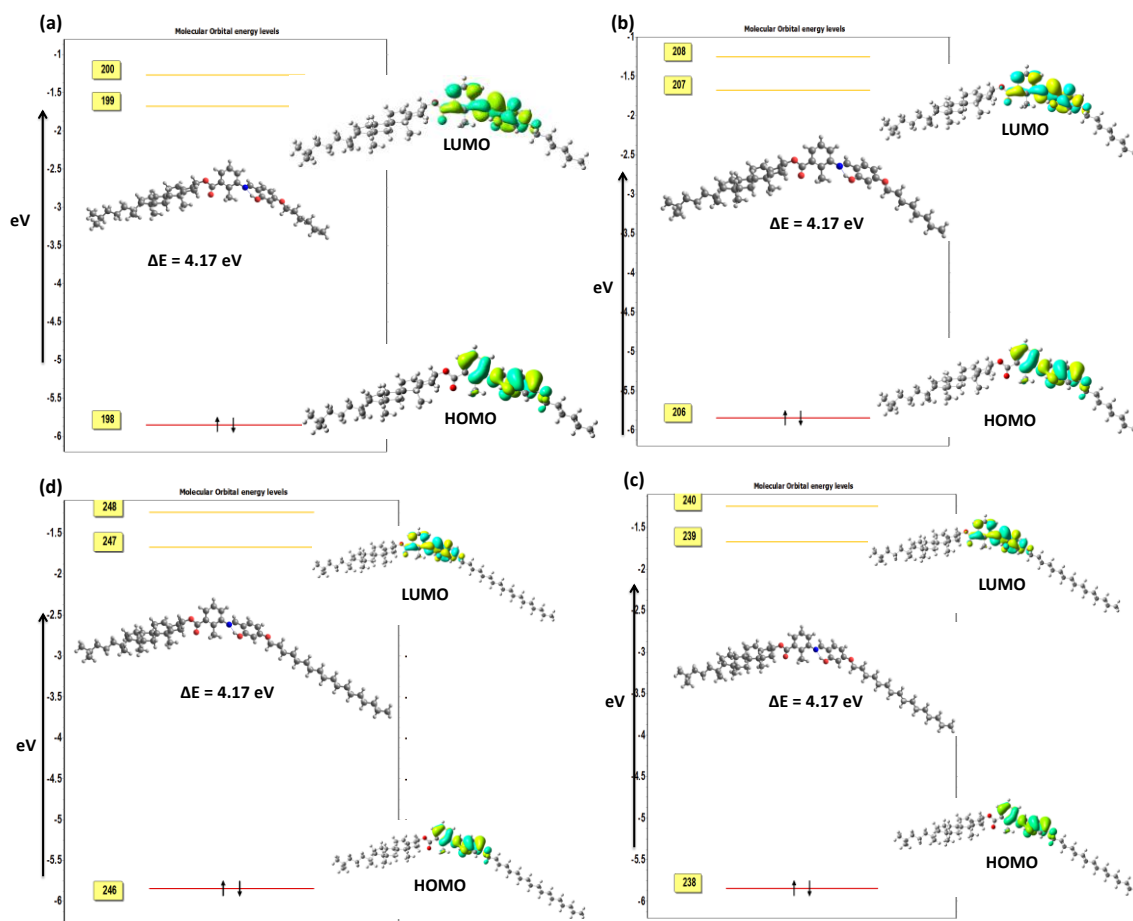


**Figure S40:** HOMO-LUMO energy gap for (a) **1-6**; (b) **1-8**; (c) **1-16** and (d) **1-18**.

All the polarizability components ( $\alpha_{xx}$ ,  $\alpha_{yy}$ ,  $\alpha_{zz}$ ) including isotropic polarizability ( $\alpha_{iso}$ ), polarizability anisotropy and asymmetry parameter calculated via DFT study for all the compounds are represented in Table S3. Polarizability component along molecular long axis ( $\alpha_{xx}$ ) is comparatively larger for all the molecules than in other two directions ( $\alpha_{yy}$ ,  $\alpha_{zz}$ ). Asymmetry parameter ( $\eta$ ), which is dependent on the bent angle, is found to be nearly same for all the three molecules. The principal component of static polarizability along the molecular long X-axis is gradually increasing from **1-6** to **1-18** in combination with the magnitude of the dipole moment values.

<b>Table S4</b>	DFT calculated principal polarizability components ( $\alpha_{xx}$ , $\alpha_{yy}$ , $\alpha_{zz}$ ), isotropic component $\alpha_{iso} = (\alpha_{xx} + \alpha_{yy} + \alpha_{zz})/3$ , anisotropy $\Delta\alpha = [\alpha_{xx} - (\alpha_{yy} + \alpha_{zz})/2]$ , and asymmetry, $\eta = [(\alpha_{yy} - \alpha_{zz}) / (\alpha_{xx} - \alpha_{iso})]$ .					
<b>Compound</b>	$\alpha_{xx}$	$\alpha_{yy}$	$\alpha_{zz}$	$\alpha_{iso}$	$\Delta\alpha$	$\eta_a$
<b>1-6</b>	897	516	417	610	430	0.345
<b>1-8</b>	928	545	433	635	439	0.382
<b>1-16</b>	1076	629	499	735	512	0.381
<b>1-18</b>	1107	652	518	759	522	0.385

Distribution of electrostatic potential surface and voltage holding ratio (VHR) values are correlated and a uniform charge distribution correlates equitably well with the high VHR of the material. The homogeneous distribution of positive electrostatic potential (ESP) does not vary among all the three molecules. The non-appearance of a negative ESP centres (red colourcentres) in the majority surface area of the molecule in the contour diagram signifies a comparatively higher VHR value. Since the ability to form cationic complexes via local electrostatic interactions gets lower in homogenously distributed partial charges and compares reasonably well with the high VHR property of the material. Hence positive ESP distribution in all the compounds indicate the applicability of it in mixtures of matrix elements of CLC based LCD and also gives an indication to the design of the molecules.

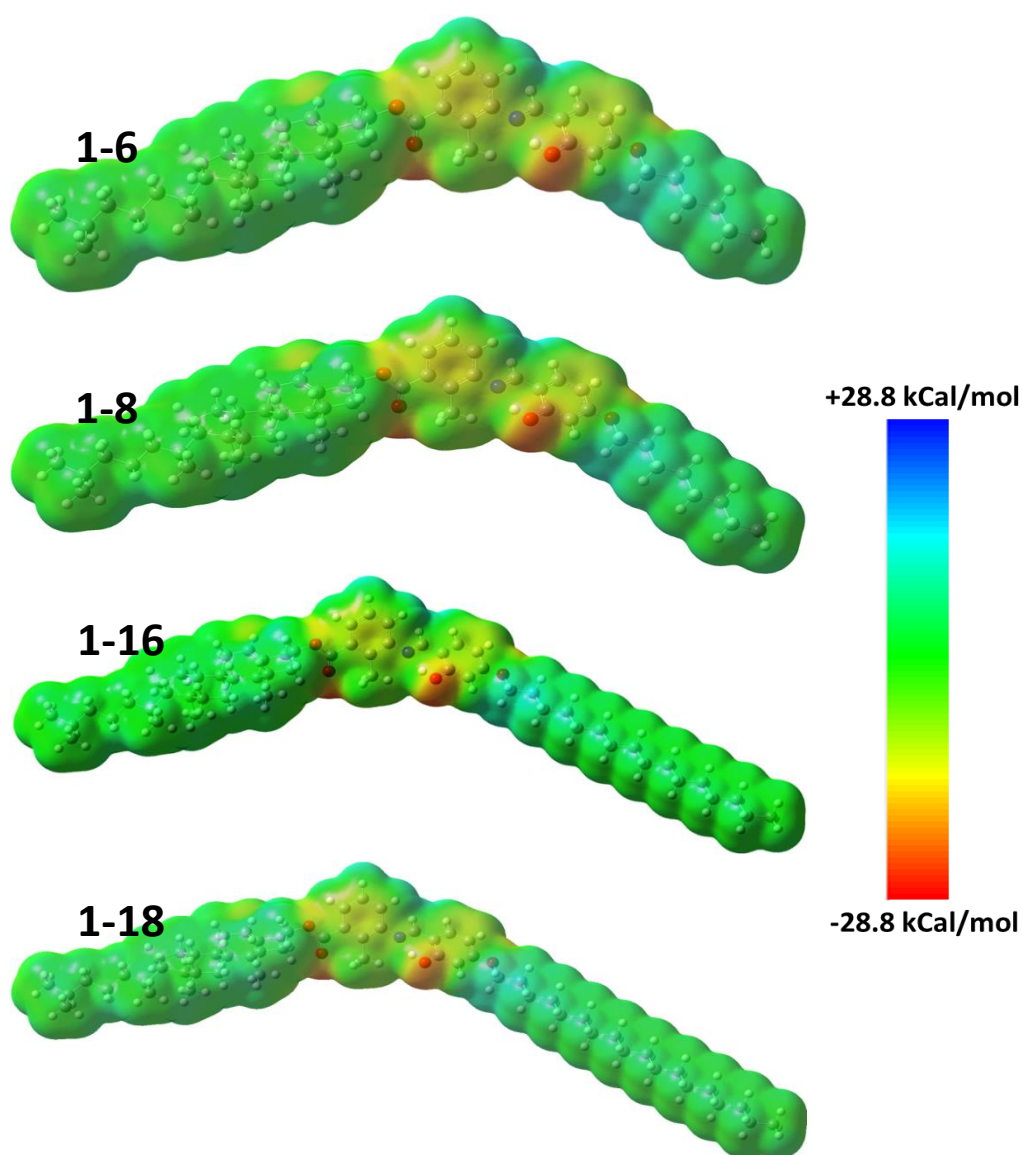


**Figure S41:** Molecular electrostatic potential distribution of 1-6, 1-8, 1-16 and 1-18

## 10. Dielectric investigations:

In order to study the relaxation dynamics of the samples we employed dielectric spectroscopy in the frequency range 20 Hz-10 MHz by using an impedance gain analyser E4990A (Keysight technologies). Different phase transition temperatures and the nature of the mesophases can be identified precisely from the dielectric study.

Dielectric investigation is carried out on the bent-core nematic samples **1-8**, **1-16** and **1-18** in planar cell of thickness 10 $\mu$ m and homeotropic cell of thickness 3.3  $\mu$ m, in the frequency range 20 Hz to 10 MHz, at various temperatures. The frequency dependence of the complex dielectric permittivity in the specified conditions is described by the superposition of the Havriliak–Negami fit function and conductivity contribution. Characteristic dielectric parameters such as dielectric strength and relaxation frequency were extracted after incorporating the dielectric data into the following extended Havriliak–Negami function equation:

$$\varepsilon'' = \frac{\sigma_0}{\varepsilon_0} \cdot \frac{1}{\omega^s} + \sum_{k=1}^N \operatorname{Im} \left\{ \frac{\Delta\varepsilon_k}{\left[ 1 + (i\omega\tau_k)^{\alpha_k} \right]^{\beta_k}} \right\} \quad (1)$$

Where  $\Delta\varepsilon_k$  is the dielectric strength and  $\tau_k$  is relaxation time of each individual process  $k$  involved in dielectric relaxation,  $\varepsilon_0$  is the vacuum permittivity (8.854 pF/m),  $\sigma_0$  is the conduction parameter and  $\omega$  is the angular frequency. The exponents  $\alpha$  and  $\beta$  are empirical fit parameters, which describe a symmetric and non-symmetric broadening, respectively, of the relaxation peaks. The first term on the right-hand side of Eq. (1) describes the motion of free charge carriers in the sample. The exponents of the angular frequency determine the non-linearity of the dc conductivity arising from charge accumulation at the interfacial layers. In the case of an Ohmic behaviour ( $s = 1$ ),  $\sigma_0$  is the Ohmic conductivity of the smectic material.

Bias variation of **1-18** reveals that peak P1 is a collective mode and P2 is a molecular mode (Figure S40(a)). The relaxation frequency of P1 increases as the voltage is increased. However the possibility of this mode being a Goldstone mode can be ruled out since the dielectric strength of this mode do not suppress at highest applied voltage (~40V) (Figure S40(b)). Thus this mode can be assigned to collective movements of molecules in SmAP<sub>A</sub> phase. As relaxation frequency of P2 does not change with bias hence it can be attributed to molecular mode.

Dielectric investigations for compound **1-8** revealed two peaks in the entire nematic range. The low frequency peak (~200Hz) arises due to fluctuations of polar clusters and has strong temperature dependence. The relaxation frequency decreases whereas dielectric strength of the peak increases upon cooling (Figure S40(c)). The other peak at higher frequency side

appears to be overlap of two different processes, one is the molecular mode for rotation of the molecules around short axis and the other is ITO relaxation.

Temperature dependence of real part of dielectric permittivity of compound **1-16** is shown in Figure S40(d). The different phases can be distinguished. The peaks are prominent in homeotropic geometry. The variation of dielectric strength and relaxation frequency of the collective mode P1 is shown in Figure S40(e).

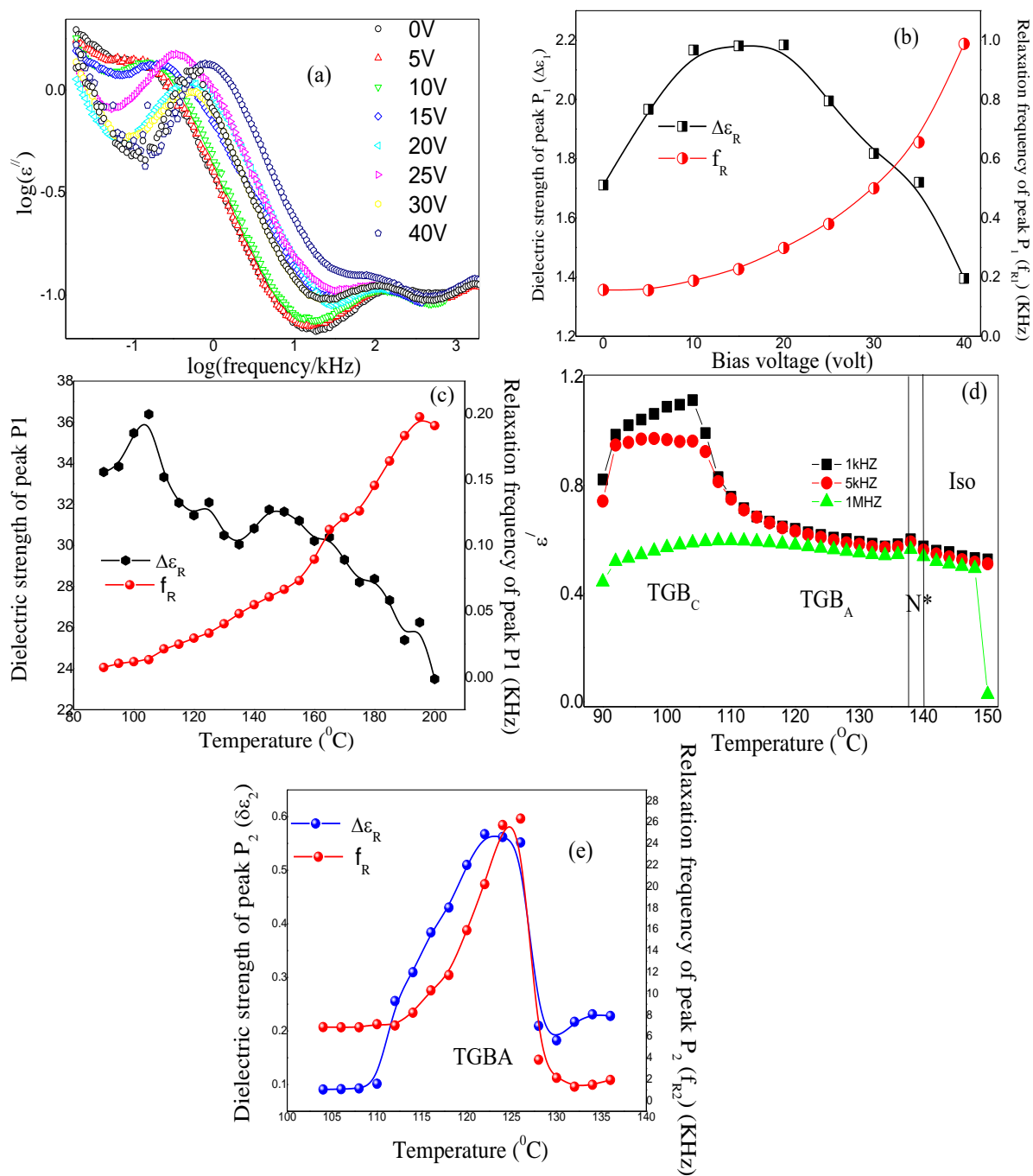


**Figure S42:** (a) Bias variation of compound **1-18**, (b) dependence of dielectric strength and relaxation frequency on bias voltage for compound **1-18**; (c) temperature dependence of dielectric strength and relaxation frequency of peak P1 of compound **1-8**; (d) real part of permittivity vs temperature for compound **1-16** in 10  $\mu\text{m}$  planar cell, (e) dependence of dielectric strength and relaxation frequency on temperature for compound **1-16** in homeotropic cell of thickness 3.3  $\mu\text{m}$ .

**Measurement of spontaneous polarization:** The switching current response was investigated using triangular wave technique for compounds **1-8**, **1-16** and **1-18**. Dependence of spontaneous polarization ( $P_S$ ) of compound **1-18** on applied voltage and frequency are shown in Figure S41.  $P_S$  increases with increasing voltage as more molecules begin switching. Beyond 40V<sub>PP</sub>  $P_S$  gets saturated. On increasing the frequency,  $P_S$  increases attains maximum around 10Hz then decreases and gets saturated.  $P_S$  vanishes beyond 50Hz as the molecules cannot follow the applied field anymore.

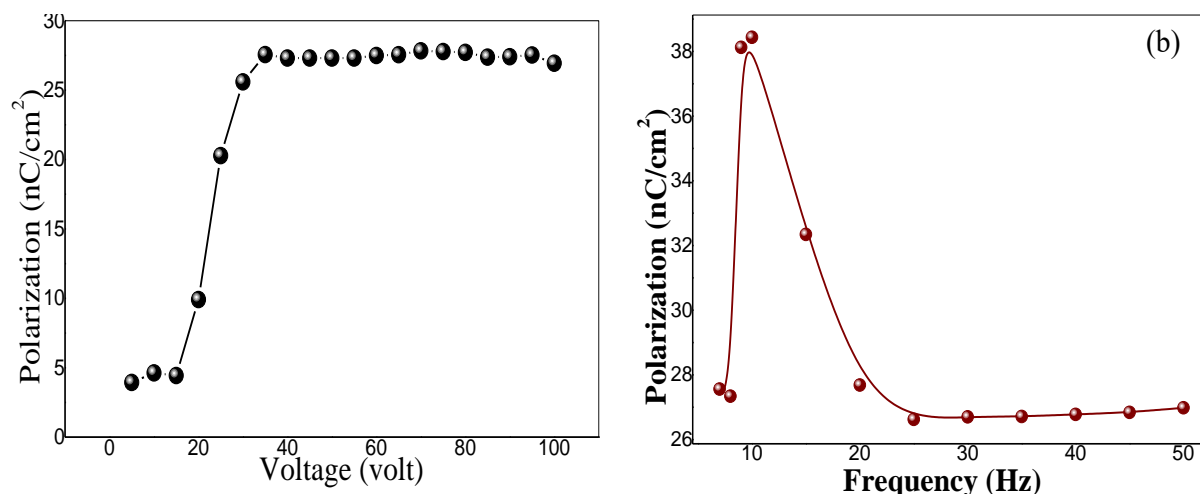


**Figure S43:** (a) Voltage variation of spontaneous polarization at frequency 20Hz, (b) frequency variation of spontaneous polarization at voltage 70V<sub>pp</sub>.

## 11. Instrumental:

Structural characterization of the compound was carried out through a combination of FT-IR (Infrared Spectroscopy-Perkin Elmer Spectrum AX3), <sup>1</sup>H-NMR and <sup>13</sup>C-NMR (Bruker Biospin Switzerland Avance-iii 400 MHz), UV-VIS-NIR spectrophotometer (LABINDIA UV-Vis Spectrophotometer 3000+) and Mass Spectrometry (Waters synapt g2s). NMR spectra were recorded using deuterated chloroform.

(CDCl<sub>3</sub>) as solvent and tetramethylsilane (TMS) as an internal standard.

Differential Scanning Calorimetry (DSC) measurements were performed on Perkin Elmer DSC 8000 coupled to a Controlled Liquid Nitrogen Accessory (CLN 2) with a scan rate of 10 °C/min.

Polarising Optical Microscopy (POM) textural observations of the mesophase were performed with Nikon Eclipse LV100POL polarising microscope provided with a Linkam heating stage (LTS 420). All images were captured using a Q-imaging camera.

X-ray Diffraction (XRD) studies were carried out on the samples using Cu K $\alpha$  ( $\lambda=1.54$  Å) radiation from GeniX3D microsource, using Pilatus 200K detector in Xeuss 2.0 SAXS/WAXS system.

## 12. References:

- [1] R. K. Nath, D. D. Sarkar, D. S. S. Rao and N. V. S. Rao, *Liq. Cryst.*, 2012, **39**, 889.-902.
- [2] C. K. Lai, C. H. Chang and C. H. Tsai, *J. Mater. Chem.*, 1998, **8**, 599-602.
- [3] D. D. Sarkar, R. Deb, N. Chakraborty and N. V. S. Rao, *Liq. Cryst.*, 2012, **39**, 1003-1010.
- [4] G. Venkatesh, K. Upadhyaya, G. Mohiuddin and N. V. S. Rao, *Liq. Cryst.*, 2013, **40**, 120-129.
- [5] Y. Kim, M. Wadab and N. Tamaoki, *J. Mater. Chem. C*, 2014, **2**, 1921-1926.
- [6] N. Tamaoki, G. Kruk and H. Matsuda, *J. Mater. Chem.*, 1999, **9**, 2381-2384.
- [7] N. Tamaoki, M. Moriyama and H. Matsuda, *Angew. Chem. Int. Ed.*, 2000, **39**, 509-511.
- [8] A. Takahashi, V. A. Mallia and N. Tamaoki, *J. Mater. Chem.*, 2003, **13**, 1582-1587.
- [9] M. Mathews and N. Tamaoki, *J. Am. Chem. Soc.*, 2008, **130**, 11409-11416.
- [10] I. Sage, *Liq. Cryst.*, 2011, **38**, 1551-1561.
- [11] H. Ocaka, B. Bilgin-Eranb, D. Güzellerb, M. Prehm and C. Tschierske, *Chem. Commun.*, 2015, **51**, 75127515.
- [12] M. J. Frisch et al., Gaussian 09, Revision B.01, Gaussian, Inc., Wallingford CT, 2010.
- [13] K. H. Kim, Y.-K. Han and J. Jung, *TheorChemAcc*, 2005, **113**, 233-237.
- [14] J. Aihara, *J. Phys. Chem. A*, 1999, **103**, 7487-7495.